

Simulating Global Dynamic Surface Reflectances for Imaging Spectroscopy Spaceborne Missions: LPJ-PROSAIL

Special Section:

The Earth in living color: spectroscopic and thermal imaging of the Earth: NASA's Decadal Survey Surface Biology and Geology Designated Observable

Benjamin Poulter¹ , Bryce Currey² , Leonardo Calle^{1,3} , Alexey N. Shiklomanov¹ , Cibele H. Amaral⁴ , E. N. Jack Brookshire² , Petya Campbell¹ , Adam Chlus⁵, Kerry Cawse-Nicholson⁵ , Fred Huemmrich¹, Charles E. Miller⁵ , Kimberley Miner⁵, Zoe Pierrat⁶ , Ann M. Raiho^{1,3}, David Schimel⁵, Shawn Serbin⁷ , William K. Smith⁸ , Natasha Stavros⁴ , Jochen Stutz⁶ , Phil Townsend⁹, David R. Thompson⁵ , and Zhen Zhang³ 

¹Biospheric Sciences Laboratory, NASA Goddard Space Flight Center, Greenbelt, MD, USA, ²Department of Land Resources and Environmental Science, Montana State University, Bozeman, MT, USA, ³Earth System Sciences Interdisciplinary Center, University of Maryland, College Park, MD, USA, ⁴Earth Lab, Cooperative Institute for Research in Environmental Sciences, University of Colorado, Boulder, CO, USA, ⁵Jet Propulsion Laboratory, California Institute of Technology, Pasadena, CA, USA, ⁶University of California Los Angeles, Los Angeles, CA, USA, ⁷Brookhaven National Laboratory, Upton, NY, USA, ⁸School of Natural Resources and the Environment, University of Arizona, Tucson, AZ, USA, ⁹University of Wisconsin, Madison, WI, USA

Key Points:

- The Earth's surface reflectance yields important information on vegetation composition, health, and productivity
- A new modeling approach is developed to simulate surface reflectance to support imaging spectroscopy missions
- The modeling approach reproduces tower-based measurements and pathfinder satellite missions and identifies areas for model improvement

Supporting Information:

Supporting Information may be found in the online version of this article.

Correspondence to:

B. Poulter,
benjamin.poulter@nasa.gov

Citation:

Poulter, B., Currey, B., Calle, L., Shiklomanov, A. N., Amaral, C. H., Brookshire, E. N. J., et al. (2023). Simulating global dynamic surface reflectances for imaging spectroscopy spaceborne missions: LPJ-PROSAIL. *Journal of Geophysical Research: Biogeosciences*, 128, e2022JG006935. <https://doi.org/10.1029/2022JG006935>

Received 28 MAY 2022

Accepted 3 JAN 2023

Corrected 17 FEB 2023

This article was corrected on 17 FEB 2023. See the end of the full text for details.

Correction added on 31 JAN 2023, after first online publication: The copyright line was changed.

© 2023 American Geophysical Union. All Rights Reserved. This article has been contributed to by U.S. Government employees and their work is in the public domain in the USA.

Abstract Spectroscopic reflectance data provide novel information on the properties of the Earth's terrestrial and aquatic surfaces. Until recently, imaging spectroscopy missions were dependent mainly on airborne instruments, such as the Next Generation Airborne Visible InfraRed Imaging Spectrometer (AVIRIS-NG), providing limited spatial and temporal observations. Currently, there is an emergence of spaceborne imaging spectroscopy missions, which require advances in end-to-end model support for traceability studies. To provide this support, the LPJ-wsl dynamic global vegetation model is coupled with the canopy radiative transfer model, PROSAIL, to generate global, gridded, daily visible to shortwave infrared (VSWIR) spectra (400–2,500 nm). LPJ-wsl variables are cross-walked to meet required PROSAIL parameters, which include leaf structure, chlorophyll *a + b*, brown pigment, equivalent water thickness, and dry matter content. Simulated spectra are compared to a boreal forest site, a temperate forest, managed grassland, a dryland and a tropical forest site using reflectance data from tower-mounted, aircraft, and spaceborne imagers. We find that canopy nitrogen and leaf-area index are the most uncertain variables in translating LPJ-wsl to PROSAIL parameters but at first order, LPJ-PROSAIL successfully simulates surface reflectance dynamics. Future work will optimize functional relationships required for improving PROSAIL parameters and include the development of the LPJ-model to represent improvements in leaf water content and canopy nitrogen. The LPJ-PROSAIL model is intended to support missions such as NASA's Surface Biology and Geology and subsequent modeled products related to the carbon cycle and hydrology.

Plain Language Summary The reflectance of the land surface provides information on vegetation composition, health, and productivity. New satellite missions are designed to better capture finely resolved reflectance information using imaging spectroscopy or hyperspectral techniques. These missions require modeling support to evaluate uncertainties. Here we present a new integrated land surface model that simulates reflectance spectra from 400 to 2,500 nm at 10 nm resolution for the entire global land surface at daily resolution. The model is evaluated using tower and pathfinder hyperspectral missions. We find that the modeling approach reproduces surface reflectance and identifies areas of model and observational improvements.

1. Introduction

The reflectance of vegetation (Gates et al., 1965; Shull, 1929), and its scaling from leaf to canopy, reveals information on vegetation health, taxonomic and functional composition, and ecosystem processes. Early vegetation indices (Kriegler et al., 1969) linked light reflectance in the red and near-infrared to chlorophyll and leaf water content (Tucker, 1979). Vegetation indices such as the Normalized Difference Vegetation Index (NDVI) have since been used to infer net primary production (NPP) and biomass accumulation (Tucker & Sellers, 1986). These indices have advanced to more precisely control for the effects of atmospheric conditions, that is, the

Author Contributions:

Conceptualization: Benjamin Poulter, Bryce Currey

Funding acquisition: Benjamin Poulter
Investigation: William K. Smith

Methodology: Benjamin Poulter, Bryce Currey, Ann M. Raiho, William K. Smith

Software: Bryce Currey, Ann M. Raiho
Supervision: Benjamin Poulter

Validation: Benjamin Poulter, Cibele H. Amaral, Jochen Stutz

Writing – original draft: Benjamin Poulter, Bryce Currey

Writing – review & editing: Benjamin Poulter, Bryce Currey

Enhanced Vegetation Index, EVI (Huete et al., 2002), or the removal of non-photosynthetic pigments, that is, the Near-Infrared Reflectance of Vegetation, NIRv (Badgley et al., 2019).

Beyond traditional two-band vegetation indices that rely on multispectral reflectance data are reflectance retrievals using imaging spectroscopy techniques (Rast & Painter, 2019). Imaging spectroscopy, also known as hyperspectral remote sensing, can resolve spectral information in ~3–10 nm increments for the visible to shortwave infrared region (VSWIR; 400–2,500 nm) and thus be integrated within a variety of modeling approaches to estimate leaf and canopy properties (Gamon et al., 2019; Wold et al., 2001). When quantified, the chemical and physical constituents of vegetation canopies, such as chlorophyll and carotenoid content, leaf dry matter, and leaf water content, can improve our understanding of terrestrial carbon, water, and energy budgets. For example, retrievals of vegetation canopy chemistry can provide insights into photosynthesis (Campbell et al., 2022), potentially reducing uncertainty in key components of the global carbon cycle, for example, where global gross primary production estimates range from 103 to 166 PgC yr⁻¹ (Norton et al., 2019).

The use of imaging spectroscopy has so far been limited mostly to airborne observations, which sample discrete spatial and temporal domains; for example, the Next Generation Airborne Visible InfraRed Imaging Spectrometer (AVIRIS-NG) instrument has been used in specific campaigns over North America, Europe, and India. Spaceborne imaging spectroscopy has been carried out via pathfinder missions such as NASA's Hyperion mission (Folkman et al., 2001; Middleton et al., 2017), the Italian Space Agency's (ASI) Hyperspectral Precursor of the Application Mission (PRISMA) (Cogliati et al., 2021; Loizzo et al., 2018), the Japanese Space Agency's Hyperspectral Imaging Suite (HISUI), and the German Aerospace Center (DLR) Earth Sensing Imaging Spectrometer, DESIS (Alonso et al., 2019; Krutz et al., 2019). These missions also tend to have limited acquisition strategies, mission duration, or do not cover the full VSWIR range.

Over the next decade, an emergence in Earth observations using imaging spectroscopy will take place; in early 2022, DLR launched the Environmental Mapping and Analysis Program (ENMAP), and in the summer of 2022, NASA launched Earth Surface Mineral Dust Source Investigation (EMIT, Connelly et al., 2021). By the end of this decade, NASA will have launched the Surface Biology and Geology (SBG) mission (Schimel & Poulter, 2022; Stavros et al., 2022), and ESA will have launched the Copernicus Hyperspectral Imaging Mission for the Environment (CHIME) mission (Nieke & Rast, 2018), providing global VSWIR retrievals at 10-nm spectral resolution, with high signal-to-noise, 30-m spatial resolution, and with potentially less than 8-days revisit when the SBG and CHIME constellation are taken together.

End-to-end (E2E) simulators will play an important role in supporting the traceability of mission requirements and in providing pre-launch characterization of expected science and applications products (Verrelst, De Grave, et al., 2021; Verrelst, Rivera-Caicedo, et al., 2021). E2E simulators quantify instrument, retrieval, and algorithmic uncertainties and the propagation of these uncertainties under various workflows. For example, the Hypertrace workflow was developed for SBG to assess science value trades and algorithm performance (Cawse-Nicholson et al., 2022; Raiho et al., 2022). Three dimensional radiative transfer models (RTMs), such as the Digital Imaging and Remote Sensing Image Generation (DIRSIG, Lentilucci & Brown, 2003; Schott et al., 1999) and Discrete Anisotropic Radiative Transfer (DART, Gastellu-Etchegorry et al., 2015), can also inform E2E as they provide a controlled simulation environment whereby surface leaving reflectances are modeled via detailed 3-dimensional representation of objects and the scattering, absorption and transmission of light (Goodenough & Brown, 2012). These approaches use ray-tracing methods that are computationally intensive and thus limited to small areas and single points in time.

Alternatively, more computationally efficient two-stream radiative transfer approximations make generalized assumptions about leaf structure (i.e., gas-like behavior) that can be used to simulate reflectance (Yuan et al., 2017). Combined with process-based models, such as land-surface models and ocean biogeochemistry models, 2-stream RTMs can also inform E2E as the basis of Observing System Simulation Experiments (OSSEs, Gelaro & Zhu, 2009). For example, ocean biogeochemical models have been coupled with RTMs to simulate water-leaving radiances in support of NASA's Plankton, Aerosols, Cloud and Ocean Ecosystem (PACE) mission instrument design and algorithm performance (Fan et al., 2021; Gregg & Rousseaux, 2017). For the land surface, the coupling of vegetation models and RTMs has been shown to produce canopy VSWIR spectra that are comparable to observations (Antonarakis et al., 2022; Shiklomanov et al., 2020) and provide insights into plant traits and chemical composition.

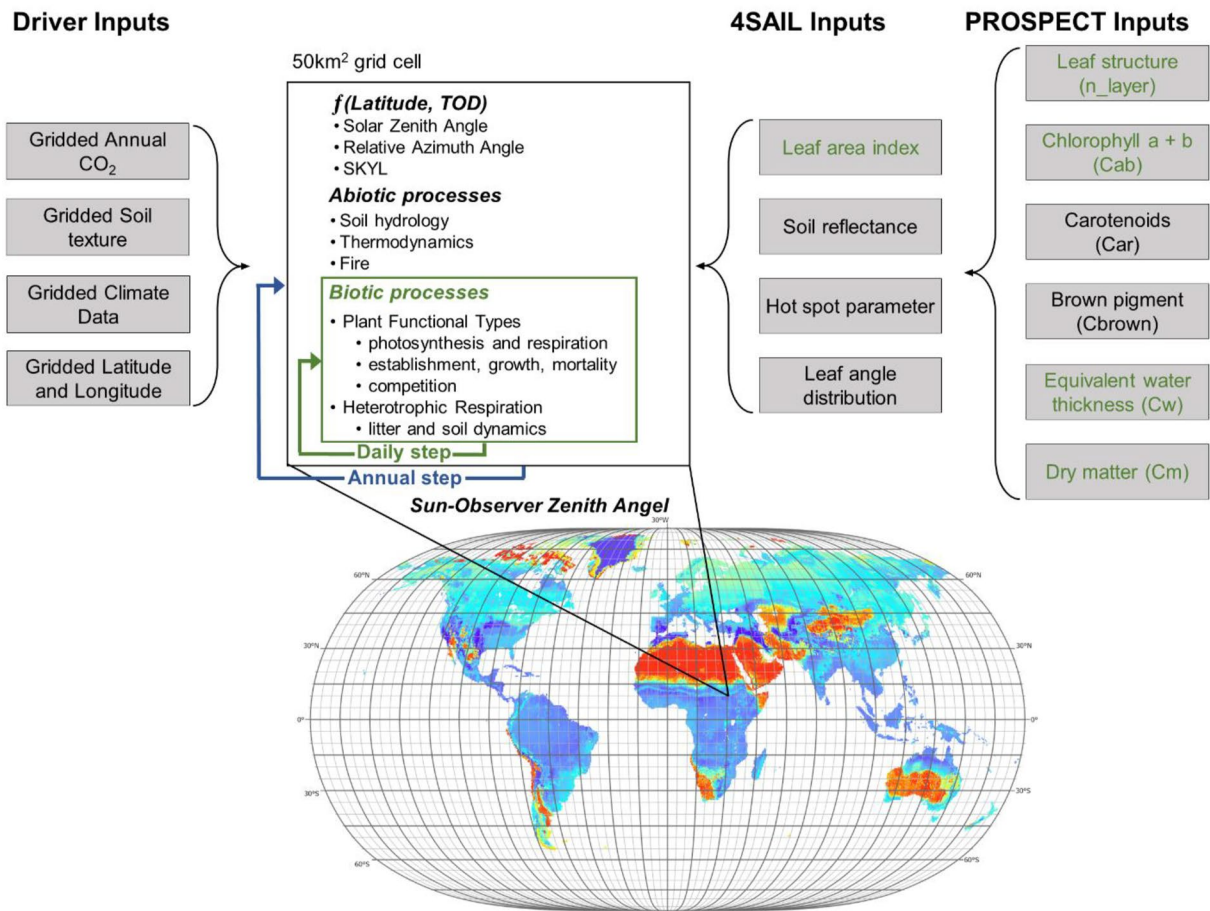


Figure 1. LPJ-PROSAIL workflow, linking drivers with LPJ processes and the PROSAIL RTM. Surface reflectances are produced via this workflow, through PROSAIL and its coupling with LPJwsl. Global grid cells in the bottom panel are exaggerated 10× for display; actual resolution is 50 km².

Here we describe the development of LPJ-PROSAIL, where LPJ is a dynamic global vegetation model (DGVM) developed for global-scale studies of vegetation dynamics and biogeochemistry (Sitch et al., 2003), and PROSAIL is a canopy radiative transfer model (Jacquemond et al., 2009) that combines leaf optical properties to simulate bidirectional reflectances. The integration of the two modeling approaches enables simulation of global scale, gridded time series of daily vegetation reflectances. We evaluate the model performance at five sites and for global applications. This activity supports NASA's SBG E2E tools and provides an opportunity to evaluate data volumes and formats, to assess instrument and algorithm performance, and to explore Level 4 mission products.

2. Methods

2.1. LPJ Dynamic Global Vegetation Model

The LPJ DGVM was developed in 2003 and couples a dynamic representation of vegetation demography with a mechanistic representation of plant physiology and biogeochemistry at a daily time step (Calle & Poulter, 2021; Sitch et al., 2003). LPJ simulates soil hydrology and vegetation dynamics in 0.5° grid cells where climate, atmospheric CO₂, and soil texture are prescribed from different driver datasets (Figure 1). A “two-bucket” soil hydrology model is coupled to stomatal conductance, via atmospheric water demand and soil-water supply, thus limiting CO₂ diffusion from the atmosphere to leaf under drought conditions (i.e., when atmospheric demand is greater than soil water supply).

Within LPJ, vegetation is categorized into 10 plant functional types (PFTs), namely tropical broad-leaved evergreen (TrBE), tropical broad-leaved raingreen (TrBR), temperate needle-leaved evergreen (TeNE), temperate broad-leaved evergreen (TeBE), temperate broad-leaved summergreen (TeBS), boreal needle-leaved evergreen

Table 1
Parameters Used in Initializing the PROSAIL Model and How They Vary by Plant Functional Type (PFT) and Time

	Var. name	Unit	Value	Variability	Source/equation
PROSPECT-5b parameter					
Leaf structure parameter	n_layer	-	$f(\text{SLA})$	PFT, daily	Jacquemond and Baret (1990)
Chlorophyll $a + b$ conc.	Cab	$\mu\text{g}/\text{cm}^2$	$f(V_{\text{cmax}})$	PFT, daily	Croft et al. (2017)
Carotenoid conc.	Car	$\mu\text{g}/\text{cm}^2$	8.0	-	Feret et al. (2008)
Brown pigment	C_{brown}	-	0.01	-	Feret et al. (2008)
Equivalent water thickness	C_w	cm	$f(\text{LAI} * \text{phen})$	PFT, daily	see Figure 2b
Dry matter content	C_m	g/cm^2	1/SLA	PFT, yearly	n/a
4SAIL parameter					
Leaf area index	LAI	-	LAI * phen	PFT, daily	Sitch et al. (2003)
Dry/wet soil reflectance	p_s	-	$f(\text{soil moisture})$	Tile, daily	Top layer soil moisture
Hotspot parameter	hspot	-	0.01	-	
Ratio of diffuse to total incident radiation	SKYL	-	0–1	Lat, DOY, time	
Solar zenith angle	tts	deg	-	Lat, DOY, time	Pierce et al. (2005)
Sun-observer zenith angle	tto	deg	0°	-	Assume nadir geometry
Relative azimuth angle	psi	deg	-	Lat, DOY, time	Pierce et al. (2005)
Distribution of leaf angles within the canopy	TypeLidf	-	1	-	Jacquemond et al. (2009)

(BeNE), boreal needle-leaved summergreen (BoNS), boreal broad-leaved summergreen (BoBS), and a C3 and C4 photosynthetic-pathway herbaceous PFT. Each PFT competes for light, space, and soil water with mortality occurring as a result of insufficient light, low growth efficiency, a negative annual carbon balance, heat stress, or when the PFT-specific bioclimatic limits are sufficiently exceeded (Sitch et al., 2003). The PFTs are characterized by leaf, fine root, sapwood and heartwood biomass pools for woody functional types and leaf and fine root pools for grasses. Photosynthesis is represented by the Farquhar biochemical model, determined as a co-limited process between maximum carboxylation capacity (V_{cmax}), electron transport (J_{max}), and sucrose utilization (Farquhar et al., 1980). V_{cmax} is estimated prognostically, as a function of photosynthetic active radiation (PAR), air temperature, and shortwave radiation, based on optimality theory to maximize photosynthesis when radiation is at its peak (Haxeltine & Prentice, 1996). Leaf area index (LAI) is estimated by integrating specific leaf area (SLA) with leaf biomass and scaled by a phenology “ramp” factor determined by growing-degree day requirements (Sitch et al., 2003). The canopy is represented as a single big leaf (Fisher et al., 2018), with no distinction for sun or shade-lit leaves and the model applies Beer’s Law to approximate vertical light profile to estimate the fraction of absorbed PAR used in photosynthesis.

Disturbances include fire, with the sub-module based on the Glob-FIRM model by Thonicke et al. (2001) and implementation is described in Sitch et al. (2003). An age-class specific land use change and landcover (LULCL) module was created and implemented by Calle and Poulter (2021) within LPJ but was not run for this initial integration with PROSAIL.

2.2. PROSAIL: The PROSPECT 5-b and 4SAIL Model

PROSAIL combines the PROSPECT 5-b generalized plate directional-hemispherical model (Feret et al., 2008) and the 4SAIL (Scattering by Arbitrary Inclined Leaves) canopy reflectance model (Verhoef et al., 2007). PROSAIL simulates canopy reflectance from 400 to 2,500 nm (at 1 nm resolution) by passing leaf optical properties (reflectance and transmittance) from PROSPECT through to 4SAIL, a four-stream radiative transfer approximation, which incorporates sun-angle geometry and filtering through a canopy. Using 14 input variables (see sections below for parameterization), six from PROSPECT-5b and eight from 4SAIL (Table 1), PROSAIL therefore links spectral variation in canopy reflectance to leaf biochemical properties, canopy architecture, and soil/vegetation interactions (Figure 2a).

PROSAIL estimates four reflectance factors for directional or hemispherically-integrated incident (incoming) and exitant (outgoing) light as a function of latitude, time of year, and time of day that are integrated across the canopy

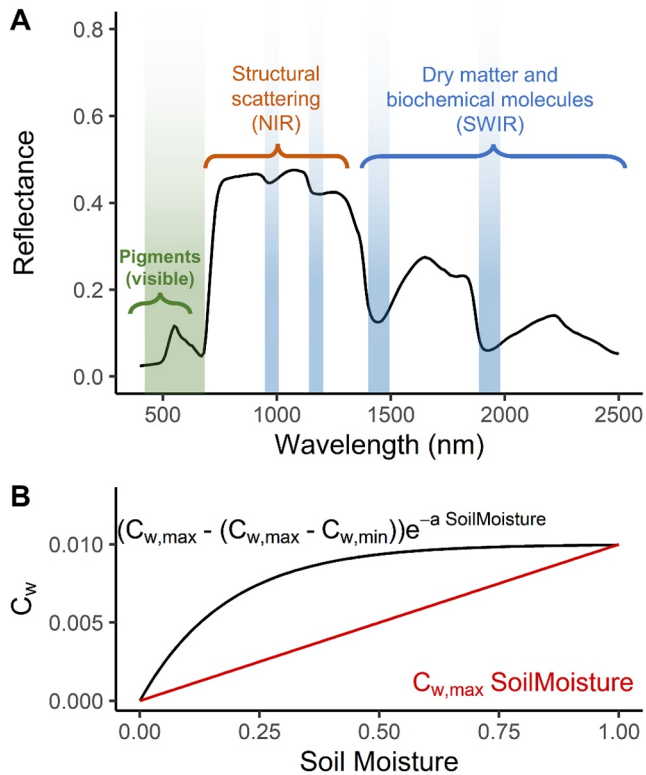


Figure 2. (a) interpretation of representative visible to shortwave infrared region spectral response and sensitivity to biochemical and structural constituents (where $N = 1.2$, $C_w = 0.009$, $Car = 8$, $Cab = 15$, $C_m = 0.005$, $C_{brown} = 0.01$), and (b) functional form selected to estimate variability in leaf water content (C_w) as a function of simulated upper layer (0–0.5 m) soil moisture. Green shading represents regions influenced by leaf nitrogen (largely due to chlorophyll $a + b$), although carotenoids and flavonoids also influence this region, and blue shading indicates wavelengths strongly influenced by water absorption.

$$SKYL = 0.847 - 1.61 \times \sin\left((90 - tts) \times \left(\frac{Pi}{180}\right)\right) + 1.04 \times \sin\left((90 - tts) \times \left(\frac{Pi}{180}\right)\right) \times \sin\left((90 - tts) \times \left(\frac{Pi}{180}\right)\right) \quad (4)$$

where E_s and E_d are wavelength-specific direct and diffuse solar irradiance ($W m^{-2} nm^{-1}$), respectively, as specified by Feret et al. (2008). These are scaled by SKYL, or the fraction of diffuse solar irradiance which itself is a function of the solar zenith angle (tts; units of degrees), defined by latitude, date, time of day, and declination. Because we assume cloud-free conditions, SKYL ranges from ~ 0.2 – 0.3 , with higher latitudes and early/late times of day resulting in a higher diffuse fraction due to longer distance of light travel through the atmosphere. This approach results in a ratio of total direct radiation to diffuse radiation roughly around 0.8. This implies that TOC_{ref} is the direct reflectance from a composite of $\sim 20\%$ diffuse incident light and $\sim 80\%$ direct incident light, as this is what most closely represents what airborne and satellite instruments actually measure.

2.3. Integrating LPJ and PROSAIL

For integration with LPJ-wsl 2.0, the PROSAIL model code was translated from Fortran 90 to C (the codebase of LPJwsl) based on <http://teledetection.ipgp.jussieu.fr/prosail/>. LPJ calls on PROSAIL sub-routines each day when vegetation is present (i.e., $LAI \Rightarrow 0$). When LAI is equal to 0, the reflectances are equal to a weighted average of (a) soil, (b) branch (if present), (c) snow (if present), or (d) mineral-surface reflectances (see next section). Five of the 14 PROSAIL inputs (Table 1) are dynamic and based on PFT-specific temporal variation (Figure 1). The eight 4SAIL parameters are derived from LAI and from latitude, day of year, and time of day. The spectral response functions are output for each

(Figure 1). The four reflectances are the pairwise combination of incident and exitant direct (i.e., directional, beam, collimated, or angle-dependent) versus diffuse (i.e., hemispherical, hemispherically-integrated, uncollimated, or angle-independent) radiation. Explicitly, the four reflectance outputs are bi-directional reflectance (BDR; i.e., direct incident, direct exitant); directional-hemispherical reflectance (DHR; i.e., direct incident, diffuse exitant), hemispherical-directional reflectance (HDR; i.e., diffuse incident, direct exitant), and bi-hemispherical reflectance (BHR; i.e., diffuse incident, diffuse exitant).

Some of the streams are insensitive to certain parameters, for example, hot-spot has no effect on the hemispherical reflectance outputs (Schaepman-Strub et al., 2006). Of importance, PROSAIL does not estimate radiance, only reflectance, thus is independent of the quality of incident light. PROSAIL does take as input the solar zenith and azimuth angles for incident light, but those only affect the incident directional reflectance outputs (DHR and BDR).

For the purpose of comparison, we simulate a fifth reflectance output from LPJ-PROSAIL: top-of-canopy outgoing directional reflectance (TOC_{ref}). While BHR is the closest representation of intrinsic surface properties, BHR is insensitive to observer zenith angle by definition. As such, to compare with airborne and satellite instrumentation, we use a combination of BDR (direct incident and exitant) and HDR (diffuse incident and direct exitant) to estimate TOC_{ref} (Equation 1). TOC_{ref} is scaled by the grid cell-specific ratio of diffuse-to-direct solar irradiance, is in the sensor direction, and is estimated as the ratio of BDR and HDR as follows:

$$TOC_{ref} = \frac{(BDR \times RAD_{dir} + HDR \times RAD_{dif})}{(RAD_{dir} + RAD_{dif})} \quad (1)$$

$$RAD_{dir} = (1 - SKYL) \times E_s \quad (2)$$

$$RAD_{dif} = (SKYL) \times E_d \quad (3)$$

grid cell at either daily or monthly timesteps. The user is provided a series of compiler flags that determine whether to run LPJ-PROSAIL (flag PROSAIL), the spectral resolution (LAMBDA_BINWIDTH), the output frequency (DAILY or MONTHLY), start year for writing, and an experimental averaging of trait values to inform PROSPECT-5b rather than area-weighted averaging of PFT, soil and snow spectra.

2.4. PROSPECT-5b: Chlorophyll Content (C_{ab})

We derive chlorophyll *a* and *b* (C_{ab}) from LPJ's prognostic PFT-specific canopy V_{cmax} ($\mu\text{mol CO}_2 \text{ m}^{-2} \text{ s}^{-1}$) based on empirical relationships between the quantities derived in Croft et al. (2017). For deciduous phenology PFTs, a 10-day running average of V_{cmax} is estimated to smooth day-to-day variability where PAR equal to zero causes V_{cmax} to drop to zero (Haxeltine & Prentice, 1996). For evergreen phenology PFTs, we assumed V_{cmax} was equal to the previous year's maximum value to avoid artifacts from the strong optimality assumption of Haxeltine and Prentice (1996), which drives V_{cmax} to zero at low temperature or low PAR values. We standardize V_{cmax} to 25°C (V_{cmax25}) using Equations 8.9 to 8.11 for C3 and C4 photosynthetic pathways from Oleson et al. (2013). For all PFTs, C_{ab} is estimated by Croft et al. (2017) as:

$$C_{ab} = \frac{(V_{cmax25} - 3.72)}{1.3} \quad (5)$$

2.5. PROSPECT-5b: Equivalent Water Thickness (C_w)

C_w is measured in units of cm, and the maximum value is around 0.01 cm (Jacquemond & Ustin, 2019). C_w is challenging to derive from land-surface models as field studies for calibration are sparse or involve scaling assumptions that are not directly comparable to modeled variables. Stand-scale metrics of field measured C_w that is, Roberts et al. (2004), show that C_w scales intrinsically with LAI, thus is a combination of canopy structure and leaf internal water, but PROSAIL requires leaf level C_w .

We instead approximate C_w from soil moisture (SM) in the uppermost soil layer of LPJ, using an exponential scaling factor ($\alpha = 5.5$) and reasonable bounds on C_w (see Figure 2b):

$$C_w = (\max C_w - (\max C_w - \min C_w)) * e^{-\alpha * \text{soilmoisture}} \quad (6)$$

where $\max C_w = 0.01$ and $\min C_w = 0$. The uncertainty of this approach is evaluated at first-order by changing the shape of the response function. Future work will calibrate this relationship for each PFT using tower or airborne measurements, or potentially incorporate plant hydraulics to get a more accurate estimate of C_w .

2.6. PROSPECT-5b: Carotenoid (C_{car}) and Brown Pigment (C_{brown})

The total carotenoid content (C_{car}) is maintained at a constant $8.0 \mu\text{g cm}^{-2}$ as in Feret et al. (2008). Leaf brown pigment (C_{brown}) is useful for discriminating between photosynthetic and non-photosynthetic (i.e., polyphenols, tannins, secondary metabolites, and defensive compounds in the leaves) light absorption within a leaf. C_{brown} is poorly defined in the literature, and its interpretation varies from, most commonly, brown pigment concentrations (such as phenols or tannins) to the color of senesced leaves (Danner et al., 2019). Therefore, we set C_{brown} to a constant value (0.01) to reduce dynamic uncertainty.

2.7. PROSPECT 5-b: Leaf Structure (n_{layer}), Dry Matter Content (C_m)

The leaf structure coefficient (n_{layer}) is the number of compact layers specifying the average number of air and cell wall interfaces within the mesophyll cells of the leaves. We vary n_{layer} based on its relationship with SLA (g cm^{-2}) and the proposed hyperbolic relationship from Jacquemond and Baret (1990) and Ceccato et al. (2002):

$$n_{layer} = \frac{(0.9 \text{ SLA} + 0.025)}{(\text{SLA} - 0.01)} \quad (7)$$

Dry matter content, C_m (g cm^{-2}), is estimated from the LPJ prescribed PFT SLA values (Sitch et al., 2003):

$$C_m = \frac{1}{\text{SLA}} \quad (8)$$

2.8. 4SAIL

4SAIL requires eight parameters related to canopy structure and to solar and viewing geometry. LAI is PFT specific and varies daily and is used directly as an input to 4SAIL. The leaf inclination distribution function (LIDF) consists of two components, average leaf slope (LIDFa) and the leaf distribution bimodality (LIDFb). We assume a spherical LIDF, with LIDFa equal to -0.35 and LIDFb equal to -0.15 (Campbell, 1990; Verhoef, 1998). The hot spot parameter (S_p), defined as the ratio of leaf width to canopy height, for our simulations, we assume to be no shadow (0.01), that is, pure hot spot, to reflect no canopy obstructions. The 4SAIL soil reflectance factor (p_s) is assumed Lambertian (see Hapke, 1981; Verhoef & Bach, 2007) and is a function of LPJ SM in the upper layer:

$$p_s = SM * R1 + (1 - SM) * R2 \quad (9)$$

where $R1$ and $R2$ are empirically-derived dry and wet soil reflectances, respectively (Feret et al., 2008).

Sun-observer viewing zenith angle (vza) is fixed to nadir, 0-degrees. Solar zenith angle (sza) and relative azimuth angle (raa) are estimated from day of year, latitude, and time of day (assuming a 10:30 a.m. local time overpass).

2.9. Reflectances for Branches, Snow, and Mineral Soil

PROSAIL does not include reflectances for woody components (branches), water, snow or ice, or mineral soils, but does incorporate soil reflectance into the reflectance estimates. When LAI is zero, PROSAIL assumes that the reflectance is composed entirely of the background/soil component. In the basic 4SAIL model (Verhoef et al., 2007) the background component is based on a soil reflectance spectrum provided by a modified version of the Hapke model that includes a SM effect and accounts for a hot spot effect, for example, Equation 9. To expand the realism of our simulation and to avoid the assumption of background reflectance only coming from soils, we instead took representative spectra for branches from the ECOSTRESS spectral library (Meerdink et al., 2019), snow from Stamnes et al. (1988), and representative mineral spectra (GDS74, quartz, tectosilicate) from the USGS spectral library (Kokaly et al., 2017) and mixed these with the spectra simulated from PROSAIL (see Figure S2 in Supporting Information S1 for the spectra). We do not include open water or ice spectra.

Representative snow spectra $>1,500$ nm was smoothed using a loess smoother due to very high noise ($k = 2$, span = 0.15). The spectra for branches, snow, and desert mineral soil are mixed with the PROSAIL spectra based on the following simple assumption that when $LAI < 1$, the PROSAIL spectra are mixed with branch or snow as follows:

$$\begin{aligned} &\text{if } LAI < 1 \text{ \& } \text{annual precipitation} > 250 \text{ mm \& } \text{snow depth} == 0 \\ &TOC_{ref} = lai * \text{canopy reflectance} + (1 - lai) * \text{branch reflectance} \end{aligned} \quad (10)$$

$$\begin{aligned} &\text{if } LAI < 1 \text{ and } \text{annual precipitation} < 250 \text{ mm \& } \text{snow depth} == 0 \\ &TOC_{ref} = lai * \text{canopy reflectance} + (1 - lai) * \text{mineral soil reflectance} \end{aligned} \quad (11)$$

$$\begin{aligned} &\text{if } LAI < 1 \text{ and } \text{snow depth} > 0 \\ &TOC_{ref} = lai * \text{canopy reflectance} + (1 - lai) * \text{snow reflectance} \end{aligned} \quad (12)$$

$$\begin{aligned} &\text{if } LAI == 0 \text{ and } \text{snow depth} == 0 \\ &TOC_{ref} = \text{soil reflectance} \end{aligned} \quad (13)$$

$$\begin{aligned} &\text{if } LAI == 0 \text{ and } \text{snow depth} > 0 \text{ (assumes soil and branches are covered)} \\ &TOC_{ref} = \text{snow reflectance} \end{aligned} \quad (14)$$

This approach assumes that (a) when snow is present, it covers branches and soil, (b) when precipitation is below 250 mm, branches are absent due to insufficient moisture and therefore soil mineral reflectance is not mixed with branch reflectance, and (c) snow does not accumulate on the vegetation canopy and only partially masks out the soil reflectance. In future, a horizontal canopy structure scheme (e.g., clumping index) will be implemented following Braghieri et al., 2021, allowing us to estimate wood area index (WAI, Kuusinen et al., 2021) to more realistically determine the branch area and contribution to reflectance (Leblanc & Chen, 2001).

2.10. Averaging Spectra to the Grid Cell

PROSAIL is applied to each PFT following the steps described previously to estimate parameters for PROSPECT-5b and 4SAIL, and the mixing of branch and snow, if present. The individual PFT spectra are then averaged together, weighting the average based on the fractional coverage of each PFT within a grid cell.

2.11. Simulations: Site Descriptions and Global Set Up

LPJ-PROSAIL was run globally at 0.5-degree spatial resolution using meteorological forcing from the Climatic Research Unit for years 1901–2020, CRUv4.05 (Harris et al., 2020) and soil data from the Harmonized World Soils Database version 2.0. The land-use change module was not used in the simulations, and thus the distribution and physiology was simulated for natural PFTs. The year 2020 was the output for evaluating the spectra. Five sites were selected for evaluation (Figures 3b–3f; Figure S1 in Supporting Information S1), these include sites equipped with canopy spectrometers and spaceborne data available from the DESIS and PRISMA imaging spectrometers. The five sites included a tropical forest, a temperate forest, temperate cropland, boreal forest, and a semi-arid desert.

The “Southern Old Black Spruce” site (SOBS) in Saskatchewan was used as a representative boreal forest (latitude/longitude: 53.98°N, 105.12°W). The SOBS site is a mixed forest stand with a stand density of ~10% larch (*Larix laricina*) and ~90% black spruce (*Picea mariana*). Canopy reflectance spectra were collected using PhotoSpec using an Ocean Optics Flame Spectrometer (400–900 nm; Grossmann et al., 2018, for full instrument description). PhotoSpec was installed atop the site's 25-m scaffolding tower and collected data from September 2018–April 2021. PhotoSpec has a narrow field of view (0.7°) and takes a representative canopy scan over 44 target locations every 30 min (Pierrat et al., 2021, 2022). 30-min representative canopy averages were filtered for clear sky conditions and averaged monthly over the entire collection period between 10:00–14:00 to reflect an approximate satellite overpass time equivalent to PROSAIL configuration.

The temperate forest site is Blackhawk Island, WI, USA (43.65°N, 89.79°W), a 73-ha island in the Wisconsin River. The island is composed of a mix of broadleaf and coniferous species, including oak (*Quercus*), maple (*Acer*), and pine (*Pinus*) species. A HySpex imaging spectrometer was used to measure full range canopy reflectance (400–2,400 nm) at 1-m spatial resolution over Blackhawk Island on eight dates during the 2018 growing season (May–October) (Chlus & Townsend, 2022).

The Beltsville site is managed by the USDA Agricultural Research Service in Beltsville, Maryland (39.03°N, 76.85°W). The local climate is temperate with hot and humid summers, long fall and typically mild winters, which strongly vary in seasonal LAI, canopy chlorophyll, and biomass patterns. The site is a 22-ha rainfed maize production field, planted annually and maintained under optimal nitrogen treatment, monitored by an eddy covariance tower. During the 2017–2020 time period, the site was instrumented with an automated canopy spectrometer system Dual FLuorescence boX (FLoX, JB Hyperspectral Devices UG, Dusseldorf, Germany; Julitta et al., 2017), collecting diurnal reflectance measurements throughout the seasons. The FLoX down-welling optics were mounted at the top of a portable platform at approximately 3 m height. The upwelling optics were positioned at nadir and maintained at 1.5 m above the canopy throughout the growing season, by lifting periodically the measurement arm as new leaves developed and the canopy grew taller, viewing a 25° field of view (Campbell et al., 2019, 2022).

The semi-arid grassland site is the Rainfall Manipulation in the Santa Rita Experimental Range experimental facility (RainManSR) near Tucson, Arizona (31.79°N, 110.90°W). The spectra used for comparison were obtained using a full spectrum ASD FieldSpec3 (Zhang et al., 2022). Measurements were pre-season (a senesced period during the driest June month before the monsoon), peak season (when NDVI peaks in early September), and post season (late September when NDVI has decreased to a winter minimum). The plots received the long-term mean annual precipitation of 384 mm (2004–2018), which is consistent with total mean annual precipitation used in model runs (Figure 3).

The tropical site is La Selva, Costa Rica (10.34°N, 84.00°E), an evergreen tropical forest where a PhotoSpec imager is located on a 40-m tower providing continuous reflectance information from 400 to 1,000 nm. The same measurement and data filtering and aggregation approach was used for this site that was developed for the SOBS site.

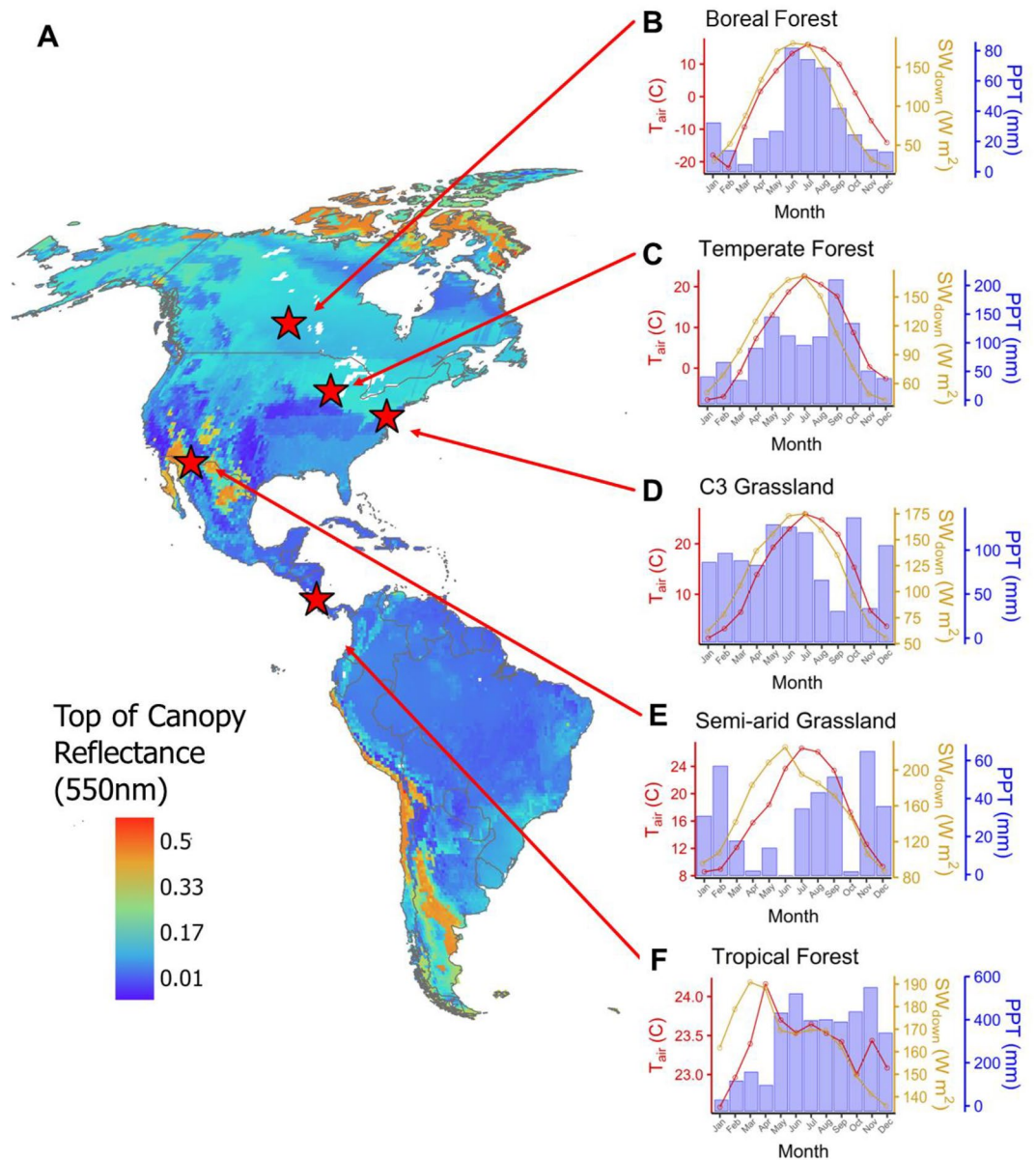


Figure 3. (a) Locations of the five intensive sites across North and Central America. The sites (b–f) were selected to be representative of temperature, moisture, and phenology gradients and for locations where tower or remote sensing data were accessible. The base map for (a) is the simulated reflectance for June at 550 nm. T_{air} is surface air temperature, SW_{down} is downward shortwave radiation, and PPT is monthly precipitation.

2.12. Remote-Sensing Observations

Two spaceborne imaging spectrometers provided hyperspectral reflectance observations, DESIS and PRISMA. We acquired the spectra for DESIS and PRISMA for three sites from teledyne.tcloudhost.com and prisma.asi.it for the months June to August of 2020 and 2021. DESIS covers the spectral range 400–1,000 nm (VNIR) with bandwidth of 3.5 nm and spectral sampling of 2.5 nm, totaling 235 channels. PRISMA covers the full VSWIR spectrum, that is, 400–2,500 nm, with bandwidth of 12 nm and spectral sampling of about 9.3 nm resulting in 240 bands. Both sensors collect data at 30-m spatial resolution. The used images were collected with clear-sky conditions over the target sites and rated as “acceptable” during the quality assessment. We downloaded surface

reflectance products processed to Levels 2A (DESI) and 2D (PRISMA) and extracted the average spectra from 2×2 pixels ($3,600 \text{ m}^2$) polygons around the site's central coordinates.

AVIRIS-NG data were used for the boreal (flight ID = ang20170817t180204) and temperate (flight ID = ang20190620t150429) forest site (Gao et al., 1993; Thompson et al., 2015). For the boreal site, atmospherically reflectance was available to download. However, the boreal forest site location was shaded by clouds in the available image, so we selected 25 evergreen spectra in the vicinity of the site and reported the average across the wavelengths. For the temperate forest site, radiance for the single site was downloaded and processed through atmospheric correction software, Imaging Spectrometer Optimal FITting (ISOFIT; Thompson et al., 2018), to obtain site-level reflectance.

2.13. Analysis

The analysis consists of qualitative and quantitative comparisons between the simulated and observed spectra. The assumptions and uncertainty for C_w functional form are evaluated. Results from the comparisons are used to evaluate model performance, assumptions for linking LPJ and PROSAIL, and to identify further research areas for field studies and theoretical developments.

3. Results and Discussion

Compared with ecosystem models that simulate reflectances internally, for example, Sellers (1985), our approach links the PROSAIL RTM with a global vegetation dynamic model. Many canopy RTMs exist and range in complexity from simpler models such as GeoSAIL (Huemrich, 2001) and SCOPE (Soil Canopy Observation Photosynthesis Energy; van der Tol et al., 2009), to more complex models such as FLIGHT (three-dimensional Forest LIGHT interaction, North, 1996). PROSAIL provides intermediate complexity, that provides mechanisms and appropriate scaling in time and space for our global applications.

3.1. Cross-Walking of LPJ to PROSAIL

We made several assumptions to provide the parameters required for PROSAIL listed in Table 1. For PROSPECT-5b, the parameters n_{layers} , C_{ab} , C_w , and C_m were estimated directly from LPJ variables, and for C_{ar} and C_{brown} , we used constant values due to lack of information. The main sources of error identified were in LAI, where values over the grassland site were unreasonably high, and in V_{cmax} , where values in the temperate forest site were lower than observed. Lower-than-normal V_{cmax} values also impart a negative influence on the C_{ab} parameter (Croft et al., 2017). These light harvesting pigments have a strong influence on the nitrogen absorption region of the spectra (Figure 2a). Assumptions in the functional forms used to approximate leaf water content were evaluated through sensitivity analysis. The mixing of spectra from snow, branch and soil assumed linear mixing with the potential to explore more complex weighting schemes in the future. From a theoretical perspective, LPJ represents canopy structure via a simplistic big-leaf approximation and Beer's Law to approximate light penetration within the canopy. In addition, scaling assumptions between LPJ and PROSAIL, that is, simplification of canopy structure by LPJ, versus representation of leaf and air space in PROSAIL, differ from one another and drive uncertainties.

3.2. Site Level Characteristics

For the individual sites, Figures 4–8, LPJ-PROSAIL simulated the full VSWIR spectral response, including the month-to-month temporal and spatial variability. The boreal site (Figure 4) showed seasonal reflectances that included a snow signal for winter months mixing with the canopy reflectances. The temperate forest site (Figure 5) showed higher seasonal variation in the spectra compared to the boreal site because of the greater abundance of deciduous PFTs. High reflectance in the red region was symptomatic of low V_{cmax} values simulated by LPJ ($30\text{--}40 \mu\text{mol CO}_2 \text{ m}^{-2} \text{ s}^{-1}$) in comparison to measured values ranging from 60 to $100 \mu\text{mol CO}_2 \text{ m}^{-2} \text{ s}^{-1}$. The temperate managed grassland (Figure 6) had less seasonal variation, and changes in the spectra were mainly from seasonality in V_{cmax} . As expected, the semi-arid grassland site (Figure 7) had lower overall reflectance and even less seasonality than the temperate site, although annual variability here would be expected to be quite high

Boreal Forest

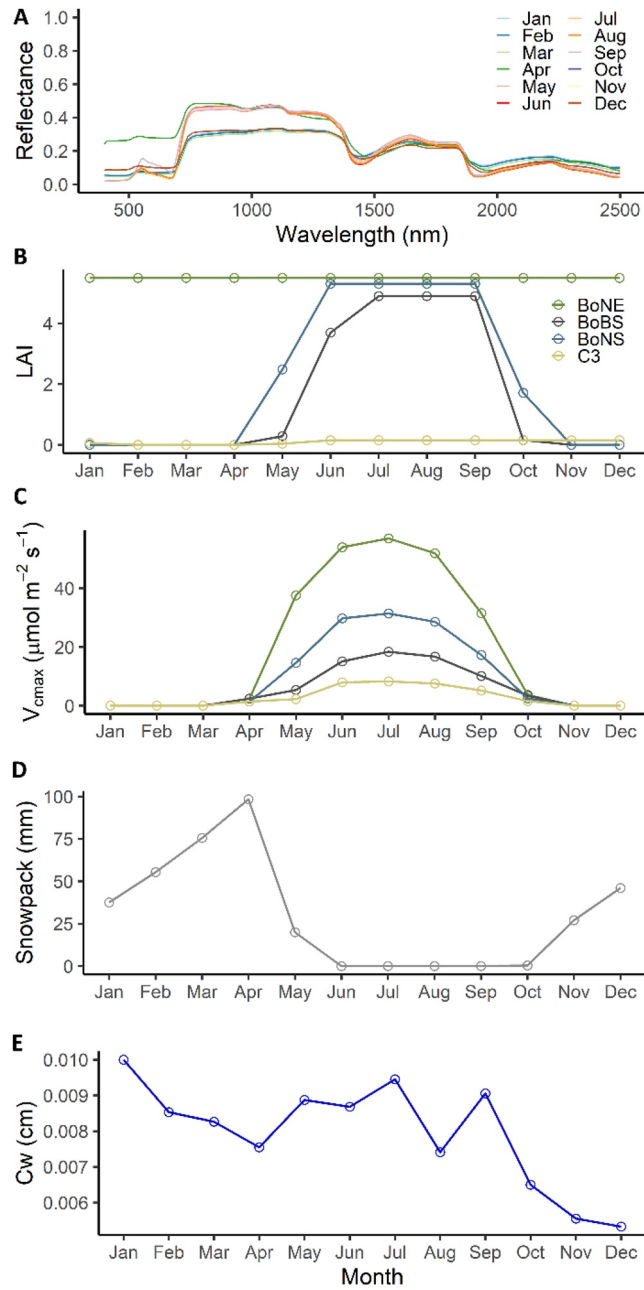


Figure 4. (a) Monthly top of canopy reflectance spectra from for the boreal evergreen forest site for 2020, (b) monthly leaf area index (LAI) for the plant functional types (PFT) location at the site, (c) monthly V_{max} for the same PFTs in (b), (d) monthly snowpack dynamics, and (e) monthly leaf water content weighted by PFT fractional area.

as the region is prone to large precipitation fluctuations. Finally, at the tropical site (Figure 8), low seasonal variation in the spectra was simulated due to a combination of little to no seasonality in LAI. Together, Figures 4–8 show that LPJ-PROSAIL captures adequate seasonal variation to inform changes in the reflectance spectra across the year.

Temperate Forest

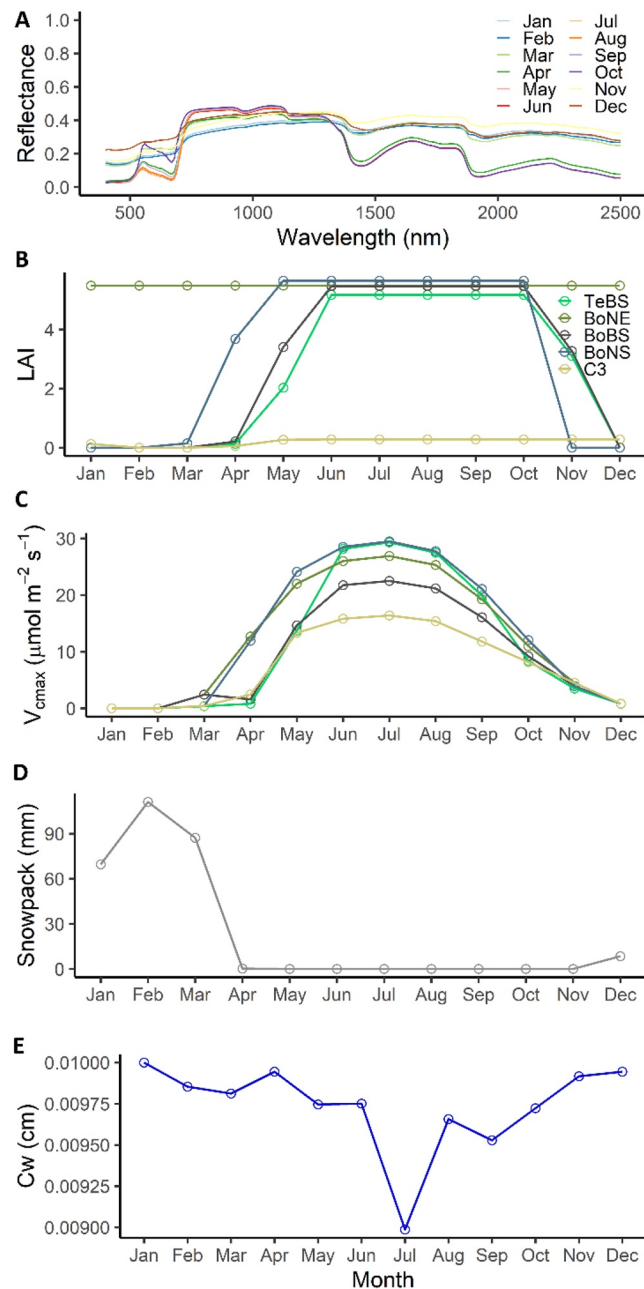


Figure 5. (a) Monthly top of canopy reflectance spectra for the temperate deciduous forest site for 2020, (b) monthly leaf area index (LAI) for the plant functional types (PFT) location at the site, (c) monthly V_{cmax} for the same PFTs in (b), (d) monthly snowpack dynamics, and (e) monthly leaf water content weighted by PFT fractional area.

Compared to observations, Figure 9 and Figure S3 in Supporting Information S1, LPJ-PROSAIL tended to have a positive bias in reflectance across the full VSWIR range. This was mainly due to the LPJ LAI being higher than what is realistic. The spectral features were generally similar to the observations from the tower, but the space-based spectra differ significantly from both model and tower reflectance and from each other. This could be related to the remote instruments' calibration or atmospheric correction; for example, sharp spectral

Temperate Grassland

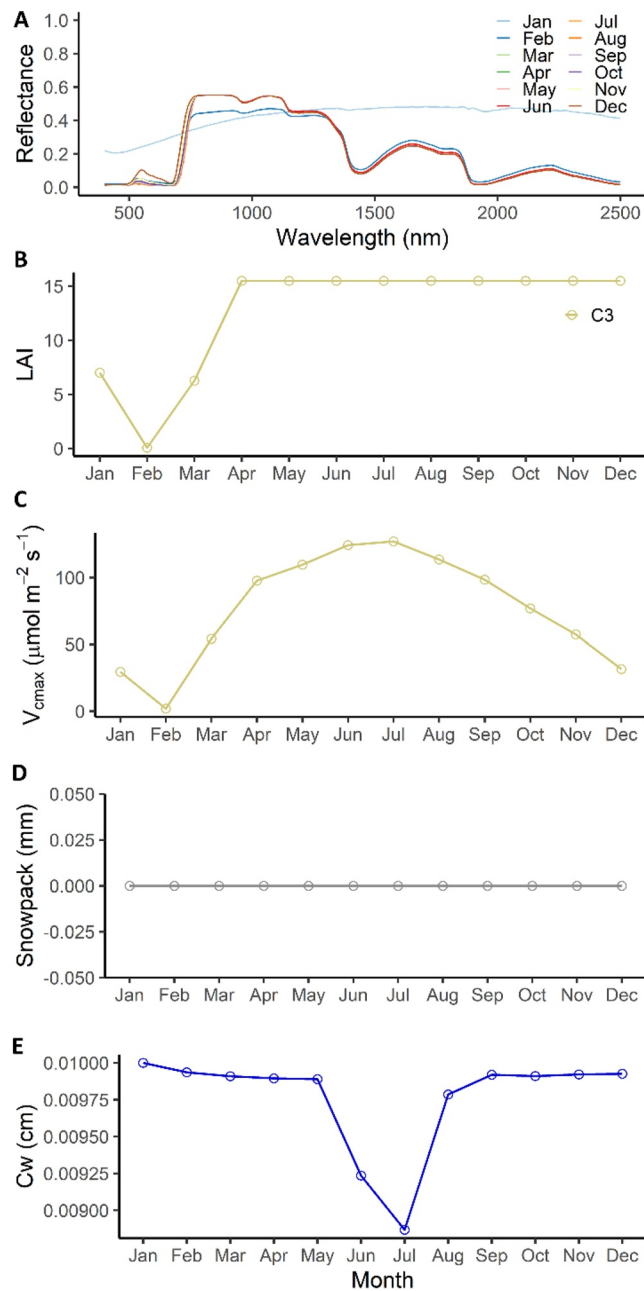


Figure 6. (a) Monthly top of canopy reflectance spectra for the temperate C3 managed grassland site for 2020, (b) monthly leaf area index (LAI) for the plant functional types (PFT) location at the site, (c) monthly V_{cmax} for the same PFTs in (b), (d) monthly snowpack dynamics, and (e) monthly leaf water content weighted by PFT fractional area.

features at 940 and 1,140 nm are likely artifacts from atmospheric water-vapor absorption. Sun-sensor viewing geometries were held constant for PROSAIL but compared to the tower observations the view angles and field of view introduce significant biases. Figure 10 uses Hoevermueller plots to illustrate how the full VSWIR spectra evolve over a representative calendar year (2020). For each site, the reflectance features show the simultaneous effects of changes in biochemistry, vegetation structure, soil, snow, and branch mixing.

Semi-arid Grassland

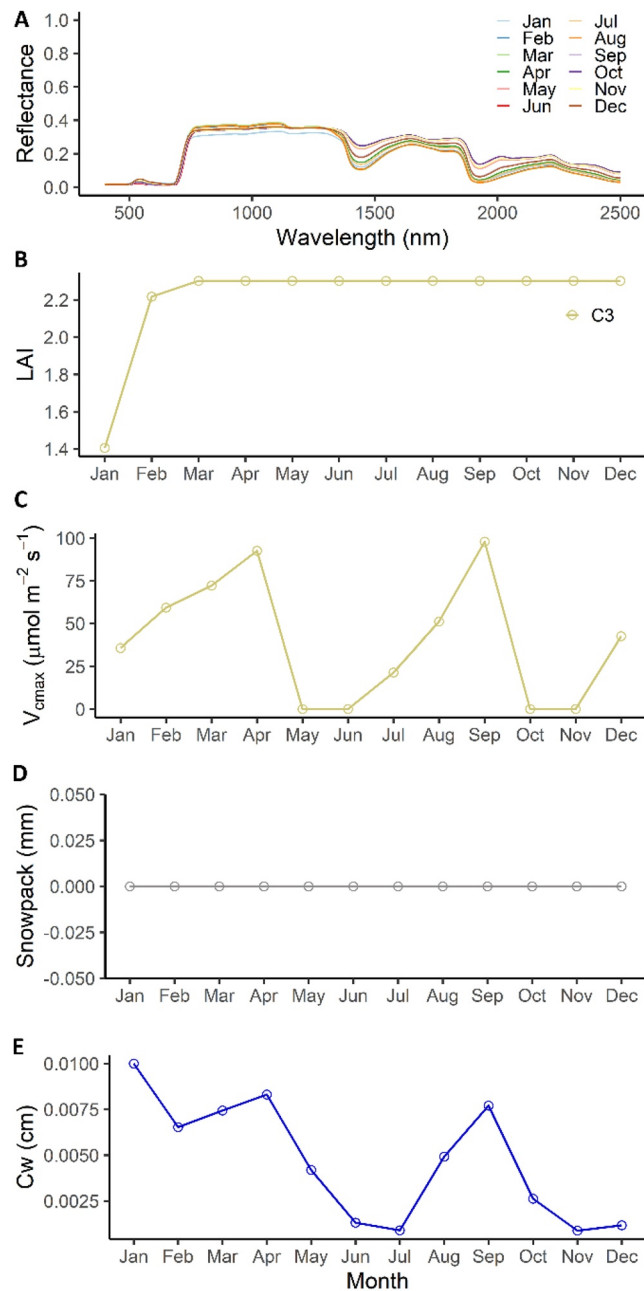


Figure 7. (a) Monthly top of canopy reflectance spectra for the semi-arid grassland site for 2020, (b) monthly leaf area index (LAI) for the plant functional types (PFT) location at the site, (c) monthly V_{cmax} for the same PFTs in (b), (d) monthly snowpack dynamics, and (e) monthly leaf water content weighted by PFT fractional area.

3.3. Sensitivity in Leaf Water Content

Figure 11 shows the biases of the spectra, representative for July 2020, in relation to how the functional form of C_w to SM is parameterized. The non-linear (default scheme used in the global simulations) shows the mid-wave infrared (MWIR) and short-wave infrared (SWIR) are most sensitive to the parameterization of the C_w . As expected, the boreal (Figure 11a) and semi-arid (Figure 11d) site are the most sensitive to the C_w parameter as they are the most water limited sites, whereas the tropical site (Figure 11e) is not sensitive to the change in functional form because SM is high enough to not affect C_w . Further work is needed to relate leaf

Tropical Forest

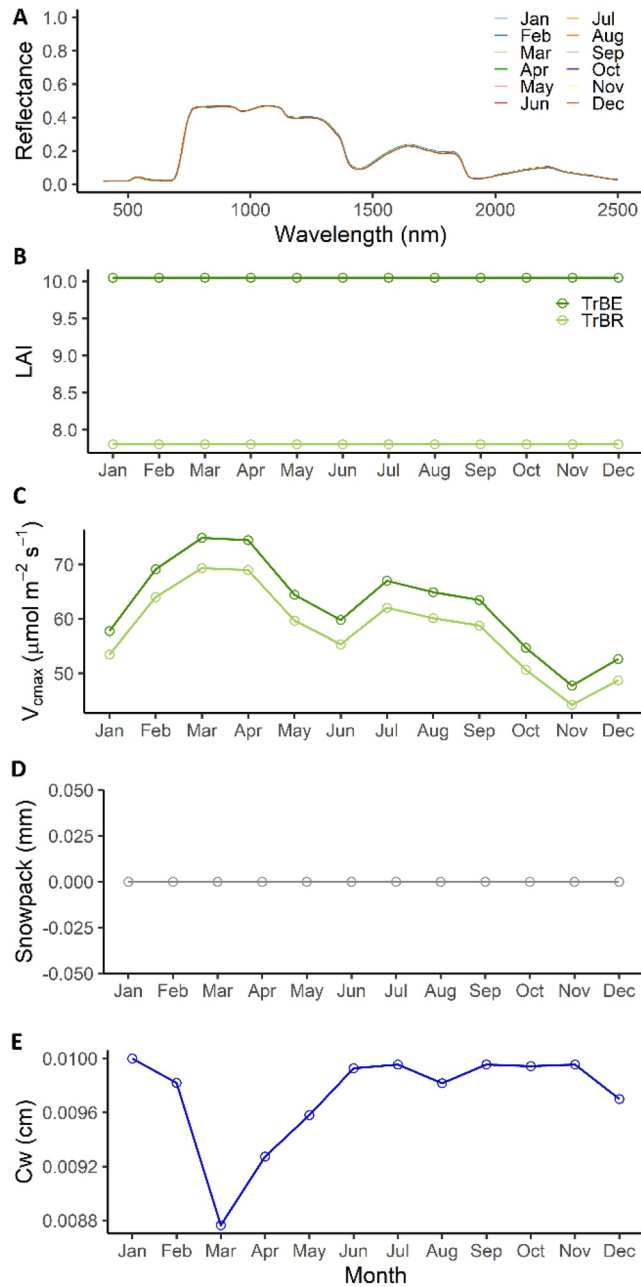


Figure 8. (a) Monthly top of canopy reflectance spectra for the tropical evergreen forest site for 2020, (b) monthly leaf area index (LAI) for the plant functional types (PFT) location at the site, (c) monthly V_{cmax} for the same PFTs in (b), (d) monthly snowpack dynamics, and (e) monthly leaf water content weighted by PFT fractional area.

moisture to fitting C_w using tower and leaf-level observations or by integrating airborne data, including radar that can retrieve canopy moisture content.

3.4. Global-Scale Characteristics

The spectral response functions and their seasonal dynamics from the five sites show that LPJ-PROSAIL captures expected variability across biomes, where phenology, SM, and seasonality are different. At the global scale, LPJ-PROSAIL simulated spectra for each grid cell, 0.5-degrees resolution, at a daily temporal resolution. These

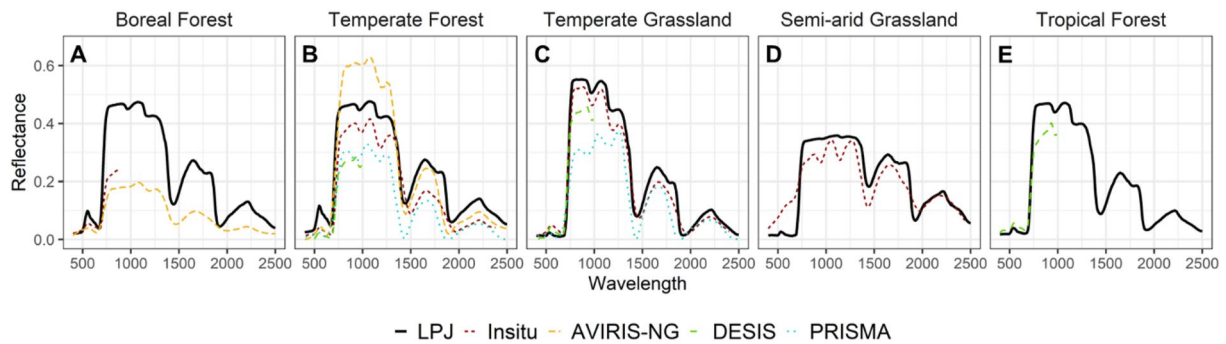


Figure 9. Comparison of August 2020 spectra for the five sites (a–e) and the available in-situ (e.g., PhotSpec, FieldSpec) and spaceborne observations (AVIRIS-NG, DESIS, PRISMA).

spectra can be used with empirical algorithms to derive canopy properties as independent verification or evaluation of the LPJ model or to be used to update model states and assess errors and uncertainties. Additionally, vegetation indices can be derived from the simulation as alternative measures for site-level evaluation or spaceborne observations. Figure 12 illustrates how LPJ-PROSAIL NDVI can be derived for the winter and summer months using $((850 \text{ nm} - 650 \text{ nm}) / (850 \text{ nm} + 650 \text{ nm}))$ and its comparison to the MOD13C2 v6.1 NDVI product. In January, snow cover and deciduous phenology lead to low NDVI in high latitudes, with fairly high NDVI in the pan-tropics. The differences between LPJ-PROSAIL and MODIS are most noticeable in the mid-latitudes, where land use and agriculture, not included in LPJ-PROSAIL, are causing differences in observed and simulated

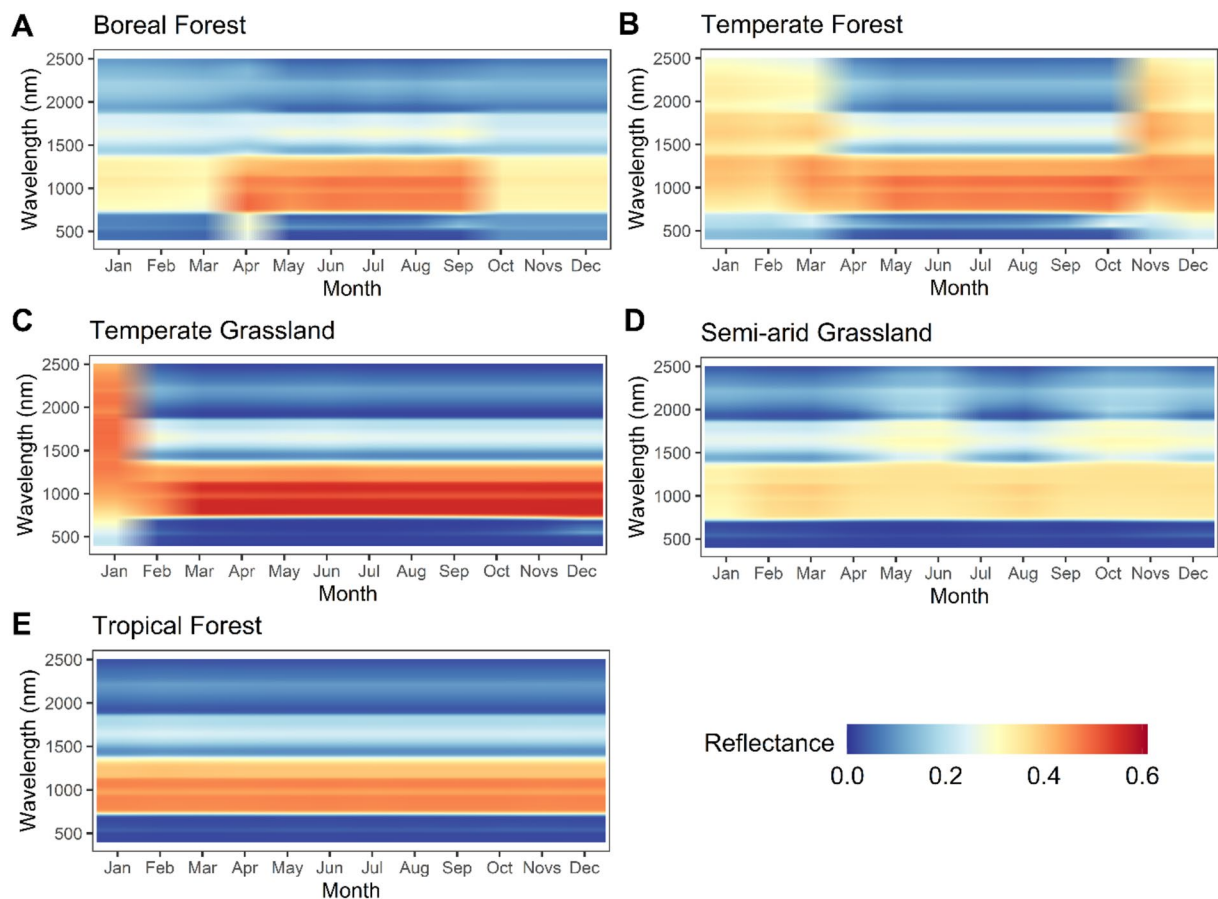


Figure 10. Hoefmueller plots illustrating the full temporal variation in spectra for each of the five sites (a–e).

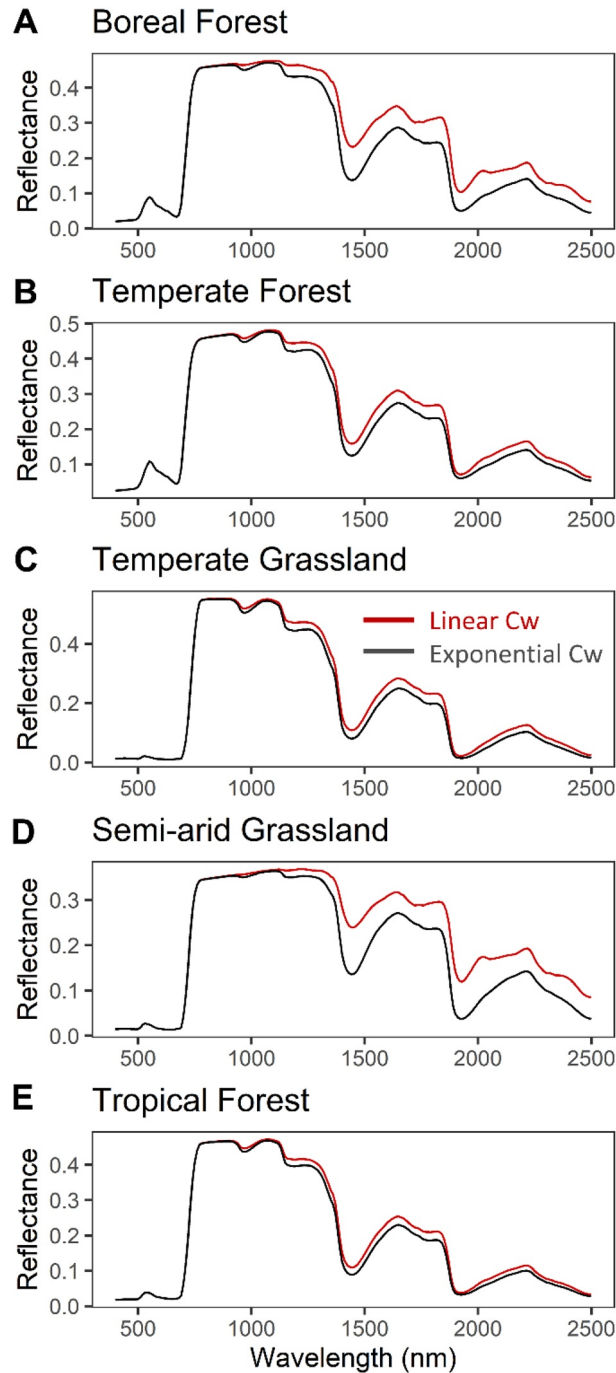


Figure 11. Spectra for two functional forms of leaf water content, C_w , for month of July 2020 for each of the five sites (a–e).

vegetation. In summer, the main differences are in the southern hemisphere sub-tropical regions, like the cerrado and miombo areas. In the winter, there is overestimation in the eastern United States and Europe, possibly due to an overestimate of LAI or PFT mismatches (e.g., too high a fraction of deciduous PFTs). A combination of land use, disturbance histories, and parameterization of LPJ PFTs are causing mismatches in phenology and can be areas of future model improvement.

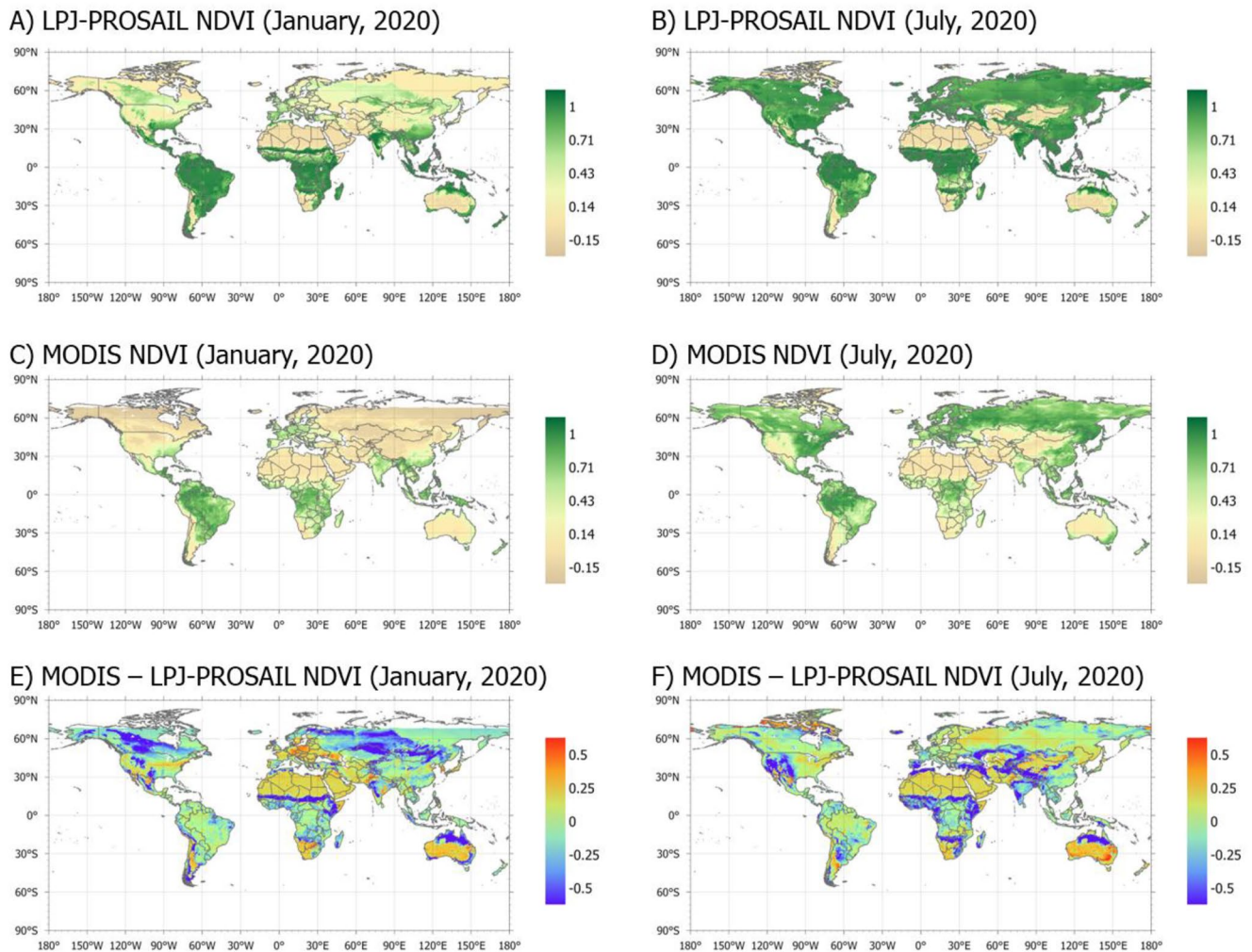


Figure 12. Derived global NDVI $((850 \text{ nm} - 650 \text{ nm}) / (850 \text{ nm} + 650 \text{ nm}))$ for 2020 January (a) and for July (b), compared to MODIS (MOD13C2 v6.1) (c, d), and the difference between MODIS and LPJ-PROSAIL (e, f). See Figure S4 in Supporting Information S1 for density plot.

3.5. E2E Applications

As imaging spectroscopy advances from targeted airborne campaigns to global spaceborne missions, there is an increasing need for advancing modeling tools to provide E2E support and to take advantage of new observations. Here, we describe the coupling of a DGVM model with the PROSAIL canopy radiative transfer model and demonstrate a simulation of global daily spectral responses. While our approach makes assumptions to match the theoretical basis of modeling approaches, the cross-walking of parameters, and functional forms, we show at first order that the spectral features and their changes over time compare well to independent observations from tower observations and from spaceborne instruments. The coupling also shows how key variables in LPJ, such as V_{cmax} and LAI, require development to be more consistent with observations.

The coupling of LPJwsl and PROSAIL has identified areas of future research to improve the cross-walking of physiological and structural parameters. Future work will consist of improving the structural representation of vegetation, the physiological parameterization, and the calibration of parameters responses using field observations. First, we intend to move beyond “big-leaf” representation to multi-layer canopy scheme (i.e., Braghieri et al., 2021) by including a clumping index to estimate horizontal structure. This approach can reduce reflectance values due to the increased scattering. This is particularly pertinent for needle-leaved canopies which can be highly clumped. This will reduce the large discrepancies between modeled versus measured reflectance from our Saskatchewan location (Figure 9a). Furthermore, this will allow us to better partition the fraction of reflectance derived from wood and branches (Leblanc & Chen, 2001).

We also intend to implement an interactive nitrogen scheme where the effects of nitrogen limitation on V_{cmax} can be better estimated and Cab can be partitioned into its separate components to better inform PROSPECT-5b. We expect these modifications to subsequently reduce reflectance values in the 400–800 nm region, which are most apparently different where needle-leaved PFTs are present (Figures 9a and 9b; Zhang et al., 2017). Functional forms of LPJ-PROSAIL parameters will be derived using tower (i.e., SpecNet) or airborne (i.e., National Ecological Observation Network, NEON) time series. Assumptions for the 4SAIL parameterization will be explored by evaluating changes in assumptions for leaf angle distributions (e.g., *LIDF*) by PFT (planophile, erectophile, plagiophile, extremophile, and uniform). Simulations will be set up to use land use, improving some of the PFT representation in heavily managed regions. The developments also enable dynamic-trait modeling to be further explored, moving away from fixed-trait modeling that many land surface models have relied on for the past two decades (Trugman, 2022; Verheijen et al., 2013). In addition, model experiments can be carried out to understand spectral responses to climate trends, climate extremes, natural disturbances such as fire, and vegetation stress to water shortages (Shiklomanov et al., 2021).

The remote-sensing comparison underscores the need for continued improvement in instrument calibration and atmospheric correction. Differences between remote and in-situ reflectances were far larger than the discrepancy between the model and in situ data. This suggests that, even if models were perfect, the remote data might not be sufficient to accurately estimate LPJ-PROSAIL parameters. Previous studies of trait measurements often rely on limited airborne campaigns with careful, manual attention to instrument calibration and atmospheric correction. Operational trait estimation on global scales will require similarly high-fidelity estimates of surface reflectance to be produced automatically. Reconciling model predictions with remote data will require continual progress to improve atmospheric correction uncertainties (LeBauer et al., 2013).

LPJ-PROSAIL creates opportunities for both informing mission design and to also enable the global Earth system modeling community to be able to take advantage of upcoming missions (Angel & McCabe, 2022). Because the LPJ model represents generalized ecosystem properties and at large spatial scales, and that the spectra measured from towers or aircraft of satellites have their own sources of uncertainty and bias, it may not be possible to perfectly match the modeled with observed. The LPJ-PROSAIL model will be used for mission support that will help quantify mission performance and improvements to the carbon and hydrologic cycles, core science focal areas for NASA's SBG mission.

Acknowledgments

We thank J.A. Biederman for their efforts as PI of the RainManSR experimental facility, the source of the semi-arid grassland spectra used in this analysis. We acknowledge support from the NASA Surface Biology and Geology Designated Observable architecture study, B.P. and W.K.S. also acknowledge support from the NASA Carbon Cycle Science program (Grant 80NSSC21K1709). SPS was partially supported by the NASA Surface Biology and Geology Designated Observable architecture study (80GSFC22TA016) and by the United States Department of Energy, Office of Science, through the Department of Energy contract No. DE-SC0012704 to Brookhaven National Laboratory. Part of the research described in this paper was carried out at the Jet Propulsion Laboratory, California Institute of Technology, under contract with the National Aeronautics and Space Administration. Government sponsorship acknowledged. This material is also based upon work supported by the National Science Foundation Graduate Research Fellowship under Grants DGE-1650604 and DGE-2034835. Any opinion, findings, and conclusions or recommendations expressed in this material are those of the authors(s) and do not necessarily reflect the views of the National Science Foundation. We thank Teledyne Brown Engineering (TBE) and the German Aerospace Center (DLR) for providing the DESIS images. We acknowledge the PRISMA Products, © of the Italian Space Agency (ASI), delivered under an ASI License to use.

Data Availability Statement

The code is available via Zenodo at <https://zenodo.org/record/7477764#.Y6XZLS-B3T8>.

References

- Alonso, K., Bachmann, M., Burch, K., Carmona, E., Cerra, D., de los Reyes, R., et al. (2019). Data products, quality and validation of the DLR Earth sensing imaging spectrometer (DESI). *Sensors*, *19*(20), 4471. <https://doi.org/10.3390/s19204471>
- Angel, Y., & McCabe, M. F. (2022). Machine learning strategies for the retrieval of leaf-chlorophyll dynamics: Model choice, sequential versus retraining learning, and hyperspectral predictors. *Frontiers of Plant Science*, *13*, 722442. <https://doi.org/10.3389/fpls.2022.722442>
- Antonarakis, A. S., Bogan, S. A., Goulden, M. L., & Moorcroft, P. R. (2022). Impacts of the 2012–2015 Californian drought on carbon, water and energy fluxes in the Californian Sierras: Results from an imaging spectrometry-constrained terrestrial biosphere model. *Global Change Biology*, *28*(5), 1823–1852. <https://doi.org/10.1111/gcb.15995>
- Badgley, G., Anderegg, L. D. L., Berry, J. A., & Field, C. B. (2019). Terrestrial gross primary production: Using NIR_v to scale from site to globe. *Global Change Biology*, *25*(11), 3731–3740. <https://doi.org/10.1111/gcb.14729>
- Braghiere, R. K., Wang, Y., Doughty, R., Sousa, D., Magney, T., Widlowski, J.-L., et al. (2021). Accounting for canopy structure improves hyperspectral radiative transfer and sun-induced chlorophyll fluorescence representations in a new generation Earth System model. *Remote Sensing of Environment*, *261*, 112497. <https://doi.org/10.1016/j.rse.2021.112497>
- Calle, L., & Poulter, B. (2021). Ecosystem age-class dynamics and distribution in the LPJ-wsl v2.0 global ecosystem model. *Geoscientific Model Development*, *14*(5), 2575–2601. <https://doi.org/10.5194/gmd-14-2575-2021>
- Campbell, G. (1990). Derivation of an angle density function for canopies with ellipsoidal leaf angle distribution. *Agricultural and Forest Meteorology*, *49*(3), 173–176. [https://doi.org/10.1016/0168-1923\(90\)90030-a](https://doi.org/10.1016/0168-1923(90)90030-a)
- Campbell, P. E. K., Huemmrich, K. F., Middleton, E. M., Alfieri, J., van der Tol, C., & Neigh, C. S. R. (2022). Using Desis and EO-1 Hyperion reflectance time series for the assessment of vegetation traits and gross primary production (GPP). In *The international archives of the photogrammetry, remote sensing and spatial information sciences, volume XLVI-1-W1-2021* (pp. 1–8). <https://doi.org/10.5194/isprs-archives-XLVI-1-W1-2021-1-2022>
- Campbell, P. E. K., Huemmrich, K. F., Middleton, E. M., Ward, L., Julitta, T., Daughtry, C., et al. (2019). Diurnal and seasonal variations in chlorophyll fluorescence associated with photosynthesis at leaf and canopy scales. *Remote Sensing*, *11*(5), 488. <https://doi.org/10.3390/rs11050488>
- Cawse-Nicholson, K., Raiho, A., Thompson, D. R., Hulley, G., Miller, C. E., Miner, K., et al. (2022). Intrinsic dimensionality as a metric for the impact of mission design parameters. *Journal of Geophysical Research: Biogeosciences*, *127*(8), e2022JG006876. <https://doi.org/10.1002/essoar.10510874.1>

- Ceccato, P., Gobron, N., Flasse, S., Pinty, B., & Tarantola, S. (2002). Designing a spectral index to estimate vegetation water content from remote sensing data: Part 1: Theoretical approach. *Remote Sensing of Environment*, 82(2), 188–197. [https://doi.org/10.1016/S0034-4257\(02\)00037-8](https://doi.org/10.1016/S0034-4257(02)00037-8)
- Chlus, A., & Townsend, P. A. (2022). Characterizing seasonal variation in foliar biochemistry with airborne imaging spectroscopy. *Remote Sensing of Environment*, 275, 113023. <https://doi.org/10.1016/j.rse.2022.113023>
- Cogliati, S., Sarti, F., Chiarantini, L., Cosi, M., Lorusso, R., Lopinto, E., et al. (2021). The PRISMA imaging spectroscopy mission: Overview and first performance analysis. *Remote Sensing of Environment*, 262, 112499. <https://doi.org/10.1016/j.rse.2021.112499>
- Connelly, D. S., Thompson, D. R., Mahowald, N. M., Li, L., Carmon, N., Okin, G. S., & Green, R. O. (2021). The EMIT mission information yield for mineral dust radiative forcing. *Remote Sensing of Environment*, 258, 112380. <https://doi.org/10.1016/j.rse.2021.112380>
- Croft, H., Chen, J. M., Luo, X., Bartlett, P., Chen, B., & Staebler, R. M. (2017). Leaf chlorophyll content as a proxy for leaf photosynthetic capacity. *Global Change Biology*, 23(9), 3513–3524. <https://doi.org/10.1111/gcb.13599>
- Danner, M., Berger, K., Woche, M., Mauser, W., & Hank, T. (2019). Fitted PROSAIL parameterization of leaf inclinations, water content and Brown pigment content for winter wheat and maize canopies. *Remote Sensing*, 11(10), 1150. <https://doi.org/10.3390/rs11101150>
- Fan, Y., Li, W., Chen, N., Ahn, J.-H., Park, Y.-J., Kratzer, S., et al. (2021). OC-SMART: A machine learning based data analysis platform for satellite ocean color sensors. *Remote Sensing of Environment*, 253, 112236. <https://doi.org/10.1016/j.rse.2020.112236>
- Farquhar, G. D., von Caemmerer, S., & Berry, J. A. (1980). A biochemical model of photosynthetic CO₂ assimilation in leaves of C₃ species. *Planta*, 149(1), 78–90. <https://doi.org/10.1007/BF00386231>
- Feret, J.-B., François, C., Asner, G. P., Gitelson, A. A., Martin, R. E., Bidet, L. P. R., et al. (2008). PROSPECT-4 and 5: Advances in the leaf optical properties model separating photosynthetic pigments. *Remote Sensing of Environment*, 112(6), 3030–3043. <https://doi.org/10.1016/j.rse.2008.02.012>
- Fisher, R. A., Koven, C. D., Anderegg, W. R. L., Christoffersen, B. O., Dietze, M. C., Farnior, C. E., et al. (2018). Vegetation demographics in Earth system models: A review of progress and priorities. *Global Change Biology*, 24(1), 35–54. <https://doi.org/10.1111/gcb.13910>
- Folkman, M., Pearlman, J., Liao, L., & Jarecke, P. (2001). EO-1/Hyperion hyperspectral imager design, development, characterization, and calibration. In *Proceedings of SPIE hyperspectral remote sensing land and atmosphere* (Vol. 4151, pp. 40–51).
- Gamon, J. A., Somers, B., Malenkovský, Z., Middleton, E. M., Rascher, U., & Schaepman, M. E. (2019). Assessing vegetation function with imaging spectroscopy. *Surveys in Geophysics*, 40(3), 489–513. <https://doi.org/10.1007/s10712-019-09511-5>
- Gao, B.-C., Heidebrecht, K. B., & Goetz, A. F. H. (1993). Derivation of scaled surface reflectances from AVIRIS data. *Remote Sensing of Environment*, 44(2–3), 165–178. [https://doi.org/10.1016/0034-4257\(93\)90014-O](https://doi.org/10.1016/0034-4257(93)90014-O)
- Gastellu-Etchegorry, J.-P., Yin, T., Lauret, N., Cajgfinger, T., Gregoire, T., Grau, E., et al. (2015). Discrete anisotropic radiative transfer (DART 5) for modeling airborne and satellite spectroradiometer and LIDAR acquisitions of natural and urban landscapes. *Remote Sensing*, 7(2), 1667–1701. <https://doi.org/10.3390/rs70201667>
- Gates, D. M., Keegan, H. J., Schleter, J. C., & Weidner, V. R. (1965). Spectral properties of plants. *Applied Optics*, 4(1), 11–20. <https://doi.org/10.1364/AO.4.000011>
- Gelaro, R., & Zhu, Y. (2009). Examination of observation impacts derived from observing system experiments (OSEs) and adjoint models. *Tellus A: Dynamic Meteorology and Oceanography*, 61(2), 179–193. <https://doi.org/10.1111/j.1600-0870.2008.00388.x>
- Goodenough, A. A., & Brown, S. D. (2012). DIRSIG 5: Core design and implementation. In *Algorithms and technologies for multispectral, hyperspectral, and ultraspectral imagery XVIII* (Vol. 8390, pp. 124–132). SPIE. <https://doi.org/10.1117/12.919321>
- Gregg, W. W., & Rousseaux, C. S. (2017). Simulating PACE global ocean radiances. *Frontiers in Marine Science*, 4, 1–19. <https://doi.org/10.3389/fmars.2017.00060>
- Grossmann, K., Frankenberger, C., Magney, T. S., Hurlock, S. C., Seibt, U., & Stutz, J. (2018). PhotoSpec: A new instrument to measure spatially distributed red and far-red solar-induced chlorophyll fluorescence. *Remote Sensing of Environment*, 216, 311–327. <https://doi.org/10.1016/j.rse.2018.07.002>
- Hapke, B. (1981). Bidirectional reflectance spectroscopy: 1. Theory. *Journal of Geophysical Research*, 86(B4), 3039–3054. <https://doi.org/10.1029/JB086iB04p03039>
- Harris, I., Osborn, T. J., Jones, P., & Lister, D. (2020). Version 4 of the CRU TS monthly high-resolution gridded multivariate climate dataset. *Scientific Data*, 7(1), 109. <https://doi.org/10.1038/s41597-020-0453-3>
- Haxeltine, A., & Prentice, I. C. (1996). BIOME3: An equilibrium terrestrial biosphere model based on ecophysiological constraints, resource availability, and competition among plant functional types. *Global Biogeochemical Cycles*, 10(4), 693–709. <https://doi.org/10.1029/96GB02344>
- Huemmerich, K. F. (2001). The GeoSail model: A simple addition to the SAIL model to describe discontinuous canopy reflectance. *Remote Sensing of Environment*, 75(3), 423–431. [https://doi.org/10.1016/S0034-4257\(00\)00184-X](https://doi.org/10.1016/S0034-4257(00)00184-X)
- Huete, A., Didan, K., Miura, T., Rodriguez, E. P., Gao, X., & Ferreira, L. G. (2002). Overview of the radiometric and biophysical performance of the MODIS vegetation indices. *Remote Sensing of Environment*, 83(1–2), 195–213. [https://doi.org/10.1016/S0034-4257\(02\)00096-2](https://doi.org/10.1016/S0034-4257(02)00096-2)
- Jacquemond, S., & Baret, F. (1990). Prospect: A model of leaf optical properties spectra. *Remote Sensing of Environment*, 34(2), 75–91. [https://doi.org/10.1016/0034-4257\(90\)90100-Z](https://doi.org/10.1016/0034-4257(90)90100-Z)
- Jacquemond, S., & Ustin, S. (2019). *Leaf optical properties*. Cambridge University Press.
- Jacquemond, S., Verhoef, W., Baret, F., Bacour, C., Zarco-Tejada, P. J., Asner, G. P., et al. (2009). PROSPECT+SAIL models: A review of use for vegetation characterization. *Remote Sensing of Environment*, 113, S56–S66. <https://doi.org/10.1016/j.rse.2008.01.026>
- Juittita, T., Burkart, A., Rossini, M., Schickling, A., Colombo, R., Rascher, U., et al. (2017). FloX: A system for automatic long-term measurements of top of canopy sun induced chlorophyll fluorescence. In *FLEX 2017 workshop, ESA-ESRIN. ESA: FLEX 2017*. Retrieved from <https://www.jb-hyperspectral.com/products/flox/>
- Kokaly, R. F., Clark, R. N., Swayze, G. A., Livo, K. E., Hoefen, T. M., Pearson, N. C., et al. (2017). *USGS spectral library version 7 (no. 1035). Data series*. U.S. Geological Survey. <https://doi.org/10.3133/ds1035>
- Kriegler, F. J., Malila, W. A., Nalepka, R. F., & Richardson, W. (1969). Preprocessing transformations and their effects on multispectral recognition. *Remote Sensing of Environment*, VI, 97.
- Krutz, D., Müller, R., Knodt, U., Günther, B., Walter, I., Sebastian, I., et al. (2019). The instrument design of the DLR Earth sensing imaging spectrometer (DESI). *Sensors*, 19(7), 1622. <https://doi.org/10.3390/s19071622>
- Kuusinen, N., Hovi, A., & Rautiainen, M. (2021). Contribution of woody elements to tree level reflectance in boreal forests. *Silva Fennica*, 55(5), 10600. <https://doi.org/10.14214/sf.10600>
- LeBauer, D. S., Wang, D., Richter, K. T., Davidson, C. C., & Dietze, M. C. (2013). Facilitating feedbacks between field measurements and ecosystem models. *Ecological Monographs*, 83(2), 133–154. <https://doi.org/10.1890/12-0137.1>
- Leblanc, S. G., & Chen, J. M. (2001). A practical scheme for correcting multiple scattering effects on optical LAI measurements. *Agricultural and Forest Meteorology*, 110(2), 125–139. [https://doi.org/10.1016/S0168-1923\(01\)00284-2](https://doi.org/10.1016/S0168-1923(01)00284-2)

- Lentilucci, E. J., & Brown, S. D. (2003). Advances in wide-area hyperspectral image simulation. In *Targets and backgrounds IX: Characterization and representation* (Vol. 5075, pp. 110–121). SPIE. <https://doi.org/10.1117/12.488706>
- Loizzo, R., Guarini, R., Longo, F., Scopa, T., Formaro, R., Facchinetti, C., & Varacalli, G. (2018). Prisma: The Italian hyperspectral mission. In *IGARSS 2018—2018 IEEE international geoscience and remote sensing symposium* (pp. 175–178). IEEE. <https://doi.org/10.1109/IGARSS.2018.8518512>
- Meerdink, S. K., Hook, S. J., Roberts, D. A., & Abbott, E. A. (2019). The ECOSTRESS spectral library version 1.0. *Remote Sensing of Environment*, 230, 111196. <https://doi.org/10.1016/j.rse.2019.05.015>
- Middleton, E. M., Campbell, P. K. E., Ong, L., Landis, D. R., Zhang, Q., Neigh, C. S., et al. (2017). Hyperion: The first global orbital spectrometer, Earth observing-1 (EO-1) satellite (2000–2017). In *2017 IEEE international geoscience and remote sensing symposium (IGARSS)* (pp. 3039–3042). IEEE. <https://doi.org/10.1109/IGARSS.2017.8127639>
- Nieke, J., & Rast, M. (2018). Towards the Copernicus hyperspectral imaging mission for the environment (CHIME). In *IGARSS 2018—2018 IEEE international geoscience and remote sensing symposium* (pp. 157–159). <https://doi.org/10.1109/IGARSS.2018.8518384>
- North, P. R. J. (1996). Three-dimensional forest light interaction model using a Monte Carlo method. *IEEE Transactions on Geoscience and Remote Sensing*, 34(4), 946–956. <https://doi.org/10.1109/36.508411>
- Norton, A. J., Rayner, P. J., Koffi, E. N., Scholze, M., Silver, J. D., & Wang, Y.-P. (2019). Estimating global gross primary productivity using chlorophyll fluorescence and a data assimilation system with the BETHY-SCOPE model. *Biogeosciences*, 16(15), 3069–3093. <https://doi.org/10.5194/bg-16-3069-2019>
- Oleson, K., Lawrence, D. M., Bonan, G. B., Drewniak, B., Huang, M., Koven, C. D., et al. (2013). Technical description of version 4.5 of the community land model (CLM).
- Pierce, K. B., Jr., Lookingbill, T., & Urban, D. (2005). A simple method for estimating potential relative radiation (PRR) for landscape-vegetation analysis. *Landscape Ecology*, 20(2), 137–147. <https://doi.org/10.1007/s10980-004-1296-6>
- Pierrat, Z., Magney, T., Parazoo, N. C., Grossmann, K., Bowling, D. R., Seibt, U., et al. (2022). Diurnal and seasonal dynamics of solar-induced chlorophyll fluorescence, vegetation indices, and gross primary productivity in the boreal forest. *Journal of Geophysical Research: Biogeosciences*, 127(2), e2021JG006588. <https://doi.org/10.1029/2021JG006588>
- Pierrat, Z., Nehemy, M. F., Roy, A., Magney, T., Parazoo, N. C., Laroque, C., et al. (2021). Tower-based remote sensing reveals mechanisms behind a two-phased spring transition in a mixed-species boreal forest. *Journal of Geophysical Research: Biogeosciences*, 126(5), e2020JG006191. <https://doi.org/10.1029/2020JG006191>
- Raiho, A., Cawse-Nicholson, K., Chlus, A., Dozier, J., Gierach, M. M., Miner, K., et al. (2022). Exploring mission design for imaging spectroscopy retrievals for land and aquatic ecosystems. *ESS Open Archive*. <https://doi.org/10.1002/essoar.10510949.1>
- Rast, M., & Painter, T. H. (2019). Earth Observation imaging spectroscopy for terrestrial systems: An overview of its history, techniques, and applications of its missions. *Surveys in Geophysics*, 40(3), 303–331. <https://doi.org/10.1007/s10712-019-09517-z>
- Roberts, D. A., Ustin, S. L., Ogunjemiyo, S., Greenberg, J., Dobrowski, S. Z., Chen, J., & Hincley, T. M. (2004). Spectral and structural measures of northwest forest vegetation at leaf to landscape scales. *Ecosystems*, 7(5), 545–562. <https://doi.org/10.1007/s10021-004-0144-5>
- Schaepman-Strub, G., Schaepman, M. E., Painter, T. H., Dangel, S., & Martonchik, J. V. (2006). Reflectance quantities in optical remote sensing—Definitions and case studies. *Remote Sensing of Environment*, 103(1), 27–42. <https://doi.org/10.1016/j.rse.2006.03.002>
- Schimmel, D., & Poulter, B. (2022). The Earth in living color. In *IEEE aerospace proceedings*.
- Schott, J. R., Brown, S. D., Raqueño, R. V., Gross, H. N., & Robinson, G. (1999). An advanced synthetic image generation model and its application to multi/hyperspectral algorithm development. *Canadian Journal of Remote Sensing*, 25(2), 99–111. <https://doi.org/10.1080/07038992.1999.10874709>
- Sellers, P. J. (1985). Canopy reflectance, photosynthesis and transpiration. *International Journal of Remote Sensing*, 6(8), 1335–1372. <https://doi.org/10.1080/01431168508948283>
- Shiklomanov, A. N., Bond-Lamberty, B., Atkins, J. W., & Gough, C. M. (2020). Structure and parameter uncertainty in centennial projections of forest community structure and carbon cycling. *Global Change Biology*, 26(11), 6080–6096. <https://doi.org/10.1111/gcb.15164>
- Shiklomanov, A. N., Dietze, M. C., Fer, I., Viskari, T., & Serbin, S. P. (2021). Cutting out the middleman: Calibrating and validating a dynamic vegetation model (ED2-PROSPECT5) using remotely sensed surface reflectance. *Geoscientific Model Development*, 14(5), 2603–2633. <https://doi.org/10.5194/gmd-14-2603-2021>
- Shull, C. A. (1929). A spectrophotometric study of reflection of light from leaf surfaces. *Botanical Gazette*, 87(5), 583–607. <https://doi.org/10.1086/333965>
- Sitch, S., Smith, B., Prentice, I. C., Arneth, A., Bondeau, A., Cramer, W., et al. (2003). Evaluation of ecosystem dynamics, plant geography and terrestrial carbon cycling in the LPJ dynamic global vegetation model. *Global Change Biology*, 9(2), 161–185. <https://doi.org/10.1046/j.1365-2486.2003.00569.x>
- Stamnes, K., Tsay, S.-C., Wiscombe, W., & Jayaweera, K. (1988). Numerically stable algorithm for discrete-ordinate-method radiative transfer in multiple scattering and emitting layered media. *Applied Optics*, 27(12), 2502. <https://doi.org/10.1364/AO.27.002502>
- Stavros, E. N., Chroné, J., Cawse-Nicholson, K., Freeman, A., Glenn, N. F., Guild, L., et al. (2022). Designing an observing system to study the surface Biology and Geology (SBG) of the Earth in the 2020s. *Journal of Geophysical Research: Biogeosciences*, 127, e2021JG006471. <https://doi.org/10.1029/2021JG006471>
- Thompson, D. R., Gao, B.-C., Green, R. O., Roberts, D. A., Dennison, P. E., & Lundeen, S. R. (2015). Atmospheric correction for global mapping spectroscopy: ATREM advances for the HypsIRI preparatory campaign. *Remote Sensing of Environment*, 167, 64–77. <https://doi.org/10.1016/j.rse.2015.02.010>
- Thompson, D. R., Natraj, V., Green, R. O., Helmlinger, M. C., Gao, B.-C., & Eastwood, M. L. (2018). Optimal estimation for imaging spectrometer atmospheric correction. *Remote Sensing of Environment*, 216, 355–373. <https://doi.org/10.1016/j.rse.2018.07.003>
- Thonicke, K., Venevsky, S., Sitch, S., & Cramer, W. (2001). The role of fire disturbance for global vegetation dynamics: Coupling fire into a dynamic global vegetation model. *Global Ecology and Biogeography*, 10(6), 661–677. <https://doi.org/10.1046/j.1466-822X.2001.00175.x>
- Trugman, A. T. (2022). Integrating plant physiology and community ecology across scales through trait-based models to predict drought mortality. *New Phytologist*, 234(1), 21–27. <https://doi.org/10.1111/nph.17821>
- Tucker, C. J. (1979). Red and photographic infrared linear combinations for monitoring vegetation. *Remote Sensing of Environment*, 8(2), 127–150. [https://doi.org/10.1016/0034-4257\(79\)90013-0](https://doi.org/10.1016/0034-4257(79)90013-0)
- Tucker, C. J., & Sellers, P. J. (1986). Satellite remote sensing of primary production. *International Journal of Remote Sensing*, 7(11), 1395–1416. <https://doi.org/10.1080/01431168608948944>
- van der Tol, C., Verhoef, W., Timmermans, J., Verhoef, A., & Su, Z. (2009). An integrated model of soil-canopy spectral radiances, photosynthesis, fluorescence, temperature and energy balance. *Biogeosciences*, 6(12), 3109–3129. <https://doi.org/10.5194/bg-6-3109-2009>

- Verheijen, L. M., Brovkin, V., Aerts, R., Bönisch, G., Cornelissen, J. H. C., Kattge, J., et al. (2013). Impacts of trait variation through observed trait–climate relationships on performance of an Earth system model: A conceptual analysis. *Biogeosciences*, *10*(8), 5497–5515. <https://doi.org/10.5194/bg-10-5497-2013>
- Verhoef, W. (1998). *Theory of radiative transfer models applied in optical remote sensing of vegetation canopies* (Ph.D. thesis) Wageningen University and Research, Netherlands.
- Verhoef, W., & Bach, H. (2007). Coupled soil–leaf–canopy and atmosphere radiative transfer modeling to simulate hyperspectral multi-angular surface reflectance and TOA radiance data. *Remote Sensing of Environment*, *109*(2), 166–182. <https://doi.org/10.1016/j.rse.2006.12.013>
- Verhoef, W., Jia, L., Xiao, Q., & Su, Z. (2007). Unified optical-thermal four-stream radiative transfer theory for homogeneous vegetation canopies. *IEEE Transactions on Geoscience and Remote Sensing*, *45*(6), 1808–1822. <https://doi.org/10.1109/TGRS.2007.895844>
- Verrelst, J., De Grave, C., Amin, E., Reyes, P., Morata, M., Portales, E., et al. (2021). Prototyping vegetation traits models in the context of the hyperspectral chime mission preparation. In *2021 IEEE international geoscience and remote sensing symposium IGARSS* (pp. 7678–7681). <https://doi.org/10.1109/IGARSS47720.2021.9554407>
- Verrelst, J., Rivera-Caicedo, J. P., Reyes-Muñoz, P., Morata, M., Amin, E., Tagliabue, G., et al. (2021). Mapping landscape canopy nitrogen content from space using PRISMA data. *ISPRS Journal of Photogrammetry and Remote Sensing*, *178*, 382–395. <https://doi.org/10.1016/j.isprsjprs.2021.06.017>
- Wold, S., Sjostrom, M., & Eriksson, L. (2001). PLS-Regression: A basic tool of chemometrics. *Chemometrics and Intelligent Laboratory Systems*, *58*(2), 109–130. [https://doi.org/10.1016/s0169-7439\(01\)00155-1](https://doi.org/10.1016/s0169-7439(01)00155-1)
- Yuan, H., Dai, Y., Dickinson, R. E., Pinty, B., Shangguan, W., Zhang, S., et al. (2017). Reexamination and further development of two-stream canopy radiative transfer models for global land modeling: Improvement of two-stream canopy model. *Journal of Advances in Modeling Earth Systems*, *9*(1), 113–129. <https://doi.org/10.1002/2016MS000773>
- Zhang, F., Biederman, J. A., Pierce, N. A., Potts, D. L., Devine, C. J., Hao, Y., & Smith, W. K. (2022). Precipitation temporal repackaging into fewer, larger storms delayed seasonal timing of peak photosynthesis in a semi-arid grassland. *Functional Ecology*, *36*(3), 646–658. <https://doi.org/10.1111/1365-2435.13980>
- Zhang, Y., Huang, J., Wang, F., Blackburn, G. A., Zhang, H. K., Wang, X., et al. (2017). An extended PROSPECT: Advance in the leaf optical properties model separating total chlorophylls into chlorophyll *a* and *b*. *Scientific Reports*, *7*(1), 6429. <https://doi.org/10.1038/s41598-017-06694-y>

Erratum

In the author contribution section of the originally published version of this article, the following information was omitted for the co-author Bryce Currey: “Conceptualization, Methodology, Software, Writing - original draft, Writing - review & editing.” The author contributions have been corrected, and this may be considered the authoritative version of record.